The Plant Cell, Vol. 30: 1353–1374, June 2018, www.plantcell.org © 2018 ASPB.

A Suppressor Screen for AGO1 Degradation by the Viral F-Box P0 Protein Uncovers a Role for AGO DUF1785 in sRNA Duplex Unwinding[OPEN]

Benoît Derrien,[a,b,1] Marion Clavel,[a,1] Nicolas Baumberger,[a] Taichiro Iki,[b,2] Alexis Sarazin,[b] Thibaut Hacquard,[a] María Rosa Ponce,[c] Véronique Ziegler-Graff,[a] Hervé Vaucheret,[d] José Luis Micol,[c] Olivier Voinnet,[b] and Pascal Genschik[a,3]

[a]Institut de Biologie Moléculaire des Plantes, Centre National de la Recherche Scientifique, Unité Propre de Recherche 2357, Conventionné avec l'Université de Strasbourg, 67084 Strasbourg, France
[b]Department of Biology, Chair of RNA biology, Swiss Federal Institute of Technology Zurich (ETH-Z), Zurich CH-8092, Switzerland
[c]Instituto de Bioingeniería, Universidad Miguel Hernández, Campus de Elche, 03202 Elche, Spain
[d]Institut Jean-Pierre Bourgin, INRA, AgroParisTech, CNRS, Université Paris-Saclay, 78026 Versailles Cedex, France

ORCID IDs: 0000-0003-1322-7362 (M.C.); 0000-0003-3459-4532 (N.B.); 0000-0002-3215-4552 (T.I.); 0000-0002-1869-5192 (A.S.); 0000-0002-1143-9743 (T.H.); 0000-0003-0770-4230 (M.R.P.); 0000-0001-8993-4587 (V.Z.-G.); 0000-0002-9986-0988 (H.V.); 0000-0002-0396-1750 (J.L.M.); 0000-0002-4107-5071 (P.G.)

In *Arabidopsis thaliana*, ARGONAUTE1 (AGO1) plays a central role in microRNA (miRNA) and small interfering RNA (siRNA)-mediated silencing and is a key component in antiviral responses. The polerovirus F-box P0 protein triggers AGO1 degradation as a viral counterdefense. Here, we identified a motif in AGO1 that is required for its interaction with the S phase kinase-associated protein1-cullin 1-F-box protein (SCF) P0 (SCF^{P0}) complex and subsequent degradation. The AGO1 P0 degron is conserved and confers P0-mediated degradation to other AGO proteins. Interestingly, the degron motif is localized in the DUF1785 domain of AGO1, in which a single point mutation (*ago1-57*, obtained by forward genetic screening) compromises recognition by SCF^{P0}. Recapitulating formation of the RNA-induced silencing complex in a cell-free system revealed that this mutation impairs RNA unwinding, leading to stalled forms of AGO1 still bound to double-stranded RNAs. In vivo, the DUF1785 is required for unwinding perfectly matched siRNA duplexes, but is mostly dispensable for unwinding imperfectly matched miRNA duplexes. Consequently, its mutation nearly abolishes phased siRNA production and sense transgene post-transcriptional gene silencing. Overall, our work sheds new light on the mode of AGO1 recognition by P0 and the in vivo function of DUF1785 in RNA silencing.

INTRODUCTION

In eukaryotes, gene silencing is crucial for development and plays major roles in response to the environment, including pathogens, as well as in epigenetic control of transposable elements. RNA silencing involves processing of double-stranded RNA (dsRNA) by the RNase III enzyme Dicer, into small RNAs (sRNAs) of 21 to 25 nucleotides in length (Ghildiyal and Zamore, 2009). All types of described sRNAs are known to associate with ARGONAUTE (AGO) proteins to form RNA-induced silencing complexes (RISCs) (Meister, 2013; Poulsen et al., 2013). These RISCs are programmed by the bound sRNAs to specifically interact with transcripts based on sequence complementarity, resulting in mRNA cleavage, translational repression, or chromatin modification.

One large class of endogenous sRNAs is the regulatory microRNAs (miRNAs) that are produced from independent transcription units (Krol et al., 2010; Bologna and Voinnet, 2014). These miRNAs repress the expression of one or more target mRNAs with complementary sequences by inhibiting mRNA translation or inducing its cleavage and degradation or by a combination of both processes. Thus, miRNAs are predicted to regulate the expression of hundreds of mRNAs, suggesting that they can control a significant proportion of the transcriptome (Leung and Sharp, 2010). Consistent with this prediction, key roles in organ patterning have been ascribed to miRNAs in invertebrates (e.g., worms and flies) and plants (Ketting et al., 2001; Vaucheret et al., 2004; Nodine and Bartel, 2010), where mutations in genes encoding miRNA pathway components cause developmental defects leading, in the worse cases, to embryonic lethality. Important functions for sRNAs have also emerged in the study of host-pathogen interactions. In particular, in the case of viral infections in plants, invertebrates and also to some extent in mammals, where populations of small interfering RNAs (siRNAs) are produced in infected cells directly by processing dsRNA molecules derived from the viral genome itself (Ding, 2010; Maillard et al., 2013; Pumplin and Voinnet, 2013).

In the model plant *Arabidopsis thaliana*, genetic and biochemical analyses have revealed that AGO1 plays a central role in

[1]These authors contributed equally to this work.
[2]Current address: Graduate School of Frontier Biosciences, Osaka University, Yamadaoka 1-3, Suita 565-0871, Osaka, Japan.
[3]Address correspondence to pascal.genschik@ibmp-cnrs.unistra.fr.
The author responsible for distribution of materials integral to the findings presented in this article in accordance with the policy described in the Instructions for Authors (www.plantcell.org) is: Pascal Genschik (pascal.genschik@ibmp-cnrs.unistra.fr).
[OPEN]Articles can be viewed without a subscription.
www.plantcell.org/cgi/doi/10.1105/tpc.18.00111

IN A NUTSHELL

Background: In plants, small RNAs (sRNAs) are widely used to regulate gene expression of both host genes and foreign nucleic acid, like viruses. sRNAs function in this way by associating with an effector protein called ARGONAUTE (AGO). sRNAs are produced as a duplex of two complementary strands. The AGO protein acts by "loading" the sRNA duplex, then removing one of the two strands and forming an RNA-induced silencing complex (RISC). The sRNA strand that remains acts as a template for RISC to recognize and cleave a complementary target RNA (mRNA transcript or viral RNA). To protect itself from this mechanism, the *Turnip yellow virus* produces the P0 protein that degrades the AGO1 protein; but how P0 recognizes AGO1 is not yet known.

Question: We wanted to know how P0 recognizes AGO1 and what host factors, if any, does it use to achieve this targeting. Using the model plant *Arabidopsis thaliana*, we employed two complementary approaches to help pinpoint amino acids in AGO1 that are important for P0 recognition.

Findings: We found that mutating one particular amino acid of AGO1 is enough to block the binding of P0 to AGO1, and therefore its degradation. Intriguingly, this particular site is not directly accessible on the surface of the protein, suggesting that AGO1 adopts different conformations, one of which is preferred by P0. Moreover, we found that the uncharacterized domain in which this amino acid is found is important for AGO1 to "shed" the complementary strand of the sRNA duplex and thus is an intrinsic part of making a functional RISC. Our study also highlights how AGO1 copes with two different types of sRNAs: Small interfering RNA duplexes that are fully complementary are not processed by the mutated AGO1, while most microRNA duplexes that are not perfectly complementary are mostly unaffected.

Next steps: We are now working on identifying other proteins that might be important for mediating the degradation of AGO1 by P0. We are also investigating the importance of the mutated AGO1 protein in the context of infection by *Turnip yellow virus* and other plant viruses.

miRNA and siRNA-directed silencing (Mi et al., 2008). AGO1 can associate with miRNAs to recognize target mRNAs via complementary base-pairing; unlike in metazoans, most plant miRNAs display extended complementarity to their target transcripts. Arabidopsis AGO1 loaded with miRNAs mediates endonucleolytic cleavage ("slicing") (Baumberger and Baulcombe, 2005), but also translational repression of target transcripts (Brodersen et al., 2008; Li et al., 2013). Moreover, AGO1 also triggers the biogenesis of secondary siRNAs (Cuperus et al., 2010; Fei et al., 2013; Borges and Martienssen, 2015). In this pathway, specific 22-nucleotide miRNA-guided AGO1 slicing of transcripts recruits SUPPRESSOR OF GENE SILENCING3 (SGS3) to the cleavage site, and RNA-DEPENDENT-RNA-POLYMERASE6 (RDR6) converts the 3′ RISC cleavage fragment into dsRNA (Peragine et al., 2004; Vazquez et al., 2004), further processed into secondary 21- and 22-nucleotide siRNAs by DICER-LIKE4 (DCL4) and DCL2, respectively, to target in *trans* other sequence-related transcripts. Depending on the precursor RNA involved, i.e., non-coding *TAS* RNAs versus protein-coding transcripts, secondary siRNAs are classified as *trans*-acting siRNAs (tasiRNAs) and phased siRNAs (phasiRNAs), respectively.

Beside its roles in endogenous silencing pathways, AGO1 is also a major player in plant antiviral silencing (Ding, 2010; Pumplin and Voinnet, 2013). Hence, upon infection, viral dsRNA produced by intramolecular RNA folding or from replication intermediate is processed by DCL4 and DCL2 into 21- and 22-nucleotide virus-derived siRNAs (vsiRNAs). Once loaded into AGO1, as well as other AGOs, primary vsiRNAs, but also RDR-generated secondary vsiRNAs, mediate antiviral silencing of viral RNA. As a counterdefensive strategy, many, if not all, viruses have acquired viral suppressors of RNA silencing (VSRs) with the ability to target different steps of the RNA silencing pathway (Pumplin and Voinnet, 2013; Csorba et al., 2015). Previous work from our laboratory and others revealed that the P0 VSR protein from polerovirus encodes an F-box protein that hijacks the host S phase kinase-associated protein1-cullin 1 (CUL1)-F-box protein (SCF) ubiquitin-protein ligase (E3) to promote the vacuolar degradation of AGO1 (Pazhouhandeh et al., 2006; Baumberger et al., 2007; Bortolamiol et al., 2007; Csorba et al., 2010; Derrien et al., 2012). Notably, AGO1 is also degraded by this pathway in a nonviral context, at least when miRNA production or stability is compromised, suggesting that the underlying mechanisms contribute to the cellular homeostasis of AGO1. Moreover, this degradation process seems conserved across kingdoms, including in mammalian cells where the main miRNA effector, AGO2, is degraded as a miRNA-free entity by selective autophagy, alongside the miRNA-processing enzyme DICER1 (Gibbings et al., 2012).

To further investigate the process of AGO1 degradation by the viral P0 F-box protein, we conducted an unbiased forward-genetic screen designed to isolate suppressors of P0 activity in parallel to targeted AGO1 alanine scanning. Both approaches independently identified that the Domain of Unknown Function 1785 (DUF1785) of AGO1 is required for P0-mediated degradation. This domain is conserved in other eukaryotic AGO proteins, and in Arabidopsis, is also required for P0-mediated degradation of AGO2, AGO4, and potentially other plant AGOs. Unlike for other *ago1* alleles carrying lesions in other domains of the protein, plants expressing the *ago1* allele with the DUF1785 mutation exhibited only mild developmental defects. Further in vitro and in vivo biochemical analyses revealed that the hitherto DUF1785 contributes to miRNA and siRNA duplex unwinding, possibly explaining why the DUF1785 *ago1* mutant allele strongly compromises phasiRNA production and the execution of sense-transgene silencing.

RESULTS

The *sup149.1* Mutation Protects AGO1, but Not Other AGOs, from P0-Mediated Protein Degradation

We previously reported that P0 expression in Arabidopsis is deleterious for plant development, most likely due to defects in the miRNA pathway caused by AGO1 degradation (Bortolamiol et al., 2007). To better characterize the mechanism by which P0 mediates AGO1 degradation, we took advantage of a transgenic line (XVE:P0) in which the P0 protein of *Turnip yellow virus* (TuYV) is expressed under the control of the β-estradiol-inducible promoter. Upon P0 induction, the growth of seedlings germinated on plates is severely impaired, an effect most visible during primary root development (Supplemental Figures 1A and 1B). We conducted a forward genetic screen for suppressors of the growth arrest mediated by P0 induction. The seeds of homozygous XVE:P0 plants were mutagenized with ethyl methanesulfonate and individuals retaining a normal root growth on vertical plates containing β-estradiol were isolated. Among 150,000 mutated M2 plants screened, 43 putative suppressors were isolated and phenotypically confirmed in M3. As expected, several P0 intragenic mutations were identified (Supplemental Figure 1C) but also other mutations in which AGO1 protein levels remained stable while retaining intact P0 expression, among which *sup149.1* is the object of this study.

In contrast to the parental XVE:P0 line, when grown in presence of β-estradiol, *sup149.1* seedlings were insensitive to P0 expression, both for primary root elongation and leaf growth (Figures 1A and 1B). Consistent with this, induction of P0 triggered AGO1 decay in the parental line, whereas AGO1 remained stable in *sup149.1* mutant plants (Figures 1A and 1C). Note that P0 mediates only the degradation of AGO1 and not the RNA helicase SDE3, a glycine-tryptophan (GW)-repeat-containing protein partner of AGO1 and facilitator of sense transgene posttranscriptional gene silencing (S-PTGS) amplification step (Garcia et al., 2012). Next, we outcrossed the XVE:P0 transgene from *sup149.1*, to replace it with the inducible cMyc-tagged P0 construct (XVE:P0-myc), which allows P0 detection by immunoblotting. We confirmed that upon cMyc-tagged P0 induction, AGO1 accumulation remained insensitive to P0 in the *sup149.1* mutant background (Supplemental Figure 1D). Notably P0 also accelerated the decay of endogenous Arabidopsis AGO2 and AGO4 proteins, regardless of the genetic background (Supplemental Figure 1D). Therefore, degradation of these additional AGOs in the *sup149.1* background, in particular, shows an AGO1-specific effect of this mutation.

AGO1 DUF1785 Is Required for P0-Mediated AGO1 Decay

To identify which mutation underlies the *sup149.1* phenotype, we used a combination of classical linkage analysis and next-generation sequencing (Schneeberger and Weigel, 2011; Candela et al., 2015). Crossing the *sup149.1* mutant in Landsberg *erecta* revealed that the mutation is dominant because heterozygous *sup149.1*/+ plants were still able to grow normally upon P0 induction. This dominance was readily explained when *sup149.1* was mapped onto *AGO1* of which it defines a new allele. The mutation is located in the 4th exon of *AGO1* and replaces a glycine by an aspartic acid at position 371 within DUF1785 (Figure 1D), the first *ago1* mutation isolated in this specific domain among the many previously described alleles (Poulsen et al., 2013). We therefore renamed the mutation *ago1-57*, according to the current nomenclature.

To validate that the resistance to P0-mediated degradation is specific to ago1-57, the XVE:P0-myc transgene was also introgressed into the *ago1-27* background in which the ago1-27 protein carries a single A994V amino acid substitution in the PIWI (P-element Induced WImpy testi) domain (Morel et al., 2002). In these plants, the ago1-27 protein remained sensitive to P0-myc-mediated degradation (Supplemental Figure 1D). Similarly, the ago1-38 mutant protein, a G186R substitution in the N-terminal domain upstream of DUF1785 (Gregory et al., 2008), was also degraded by P0-myc in transient expression assays (Supplemental Figure 1E). This suggests that AGO1 only resists P0-myc-mediated decay in the context of the *ago1-57* mutation.

It was previously shown that the ND-PAZ domain of AGO1 is destabilized in presence of P0 (Baumberger et al., 2007) and therefore contains an AGO1 "degron," i.e., the minimal element within a protein that is sufficient for recognition and degradation by a proteolytic apparatus (Varshavsky, 1991). Interestingly, the DUF1785 carrying the *ago1-57* lesion is contained within the ND-PAZ region (Figure 2A). To further narrow down the AGO1 degron, we transiently expressed in *Nicotiana benthamiana* leaves different AGO1 deletion constructs covering these domains fused to GFP, in the absence or presence of P0-myc (Figure 2B). The ND and DUF1785 domains together (NDΔC1) conferred P0-myc-mediated degradation, unlike a similar construct missing the C-terminal part of DUF1785 (NDΔC2). Conversely, when deletions were introduced from the N-terminal part of the ND-PAZ region (ΔN1PAZ and ΔN2PAZ), the one containing the most C-terminal moieties of DUF1785 (ΔN1PAZ) displayed optimal degradation by P0-myc. Accordingly, a strongly expressed construct covering most of DUF1785 (ΔNΔC) was sufficient for P0-mediated degradation. Further comparing the boundaries of degradable versus nondegradable deletion constructs narrowed down the AGO1 degron to a sequence of approximately 18 amino acids within DUF1785 (Figures 2B and 2C).

To further identify which, among the 18 residues of the AGO1 degron, are essential for P0 action, we conducted an alanine scanning mutagenesis within the region conferring degradability to the ΔNΔC construct (Figure 2B). Each of the mutant variants was expressed in *N. benthamiana* leaves in the absence or presence of P0-myc. Three point mutations (G8A, L11A, and N12A) abolished P0-mediated degradation (Figure 2D), among which G8A matches the position of *ago1-57* in the full-length AGO1 context, a glycine conserved in all Arabidopsis AGOs (Figure 2C). We thus created an equivalent to *ago1-57* in the context of AGO2 by exchanging a glycine, G352, for an aspartate residue. As seen in the AGO1 context, the G352D mutation fully stabilized venus-AGO2 upon P0 induction (Figure 2E), underscoring the importance of this conserved residue for P0-mediated degradation of AGO proteins. While the critical glycine at position 8 of the Arabidopsis AGO1 degron is only found in plant species, the degron itself, and more broadly the DUF1785, is well conserved beyond the green lineage (Supplemental Figure 2A).

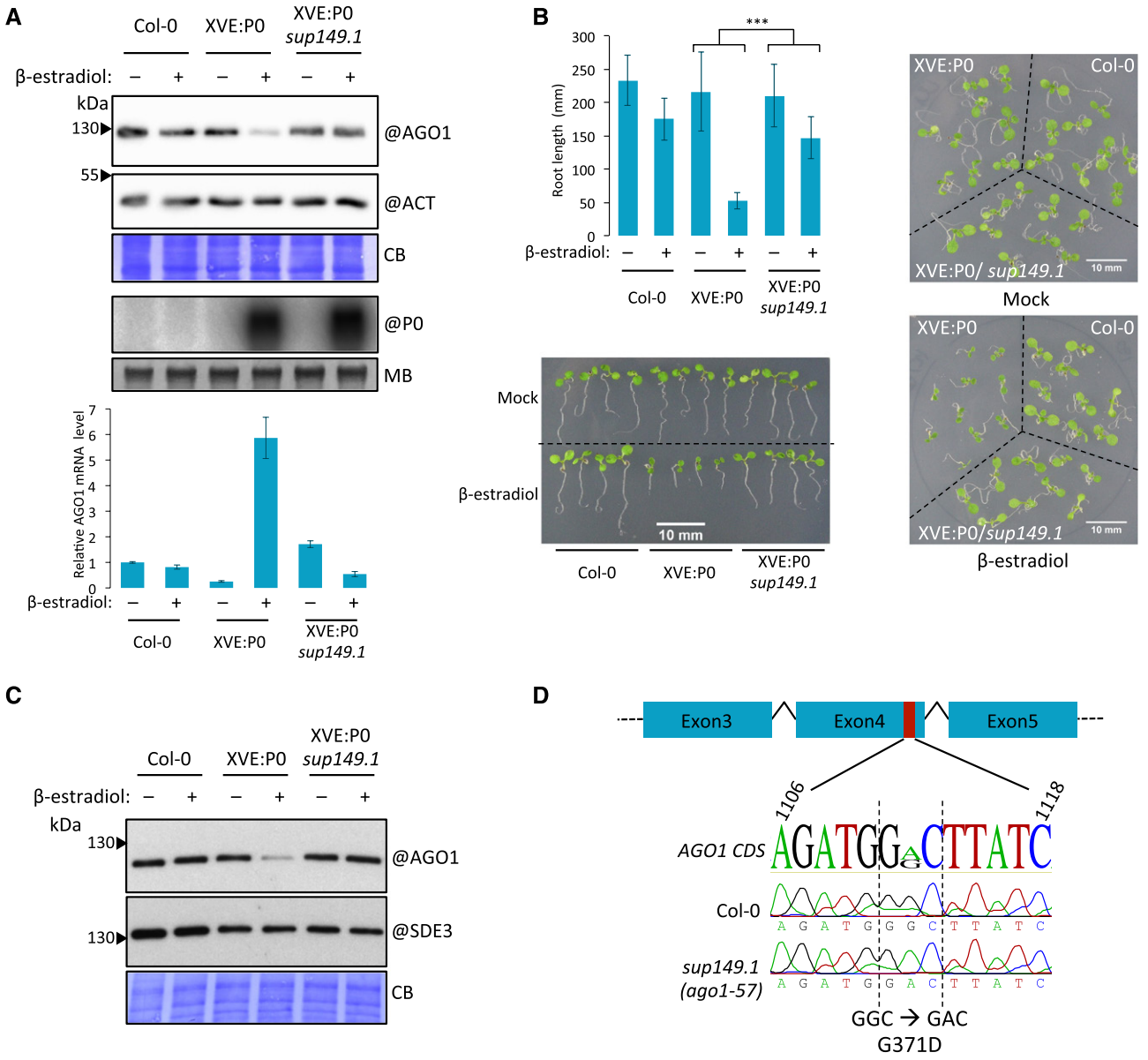

Figure 1. AGO1 in the *sup149.1* Mutant Is Insensitive to P0-Mediated Degradation.

(A) Top panel: Immunoblot analysis of AGO1 content in mock (–) or P0 induced (+) 7-d-old seedlings, grown on horizontal solid medium, with or without β-estradiol. Probing with the ACTIN antibody and Coomassie blue (CB) staining were used as loading controls. Middle panel: P0 expression is measured by RNA gel blot; loading control is shown by staining the membrane with methylene blue (MB). Bottom panel: *AGO1* mRNA level in the same samples measured by RT-qPCR. Levels are displayed relative to Col-0. "@" indicates hybridization with antibody or DNA probe.
(B) Top panel: Root length measurement of vertically grown seedlings, after 9 d on either mock (–) or β-estradiol containing (+) medium. ANOVA was performed to compare genotypes and treatment, $P < 0.001$. Bottom panel: Representative individual seedlings in mock or P0 induced condition, after 7 d. Right panel: Representative individual seedlings in mock or P0 induced conditions, after 9 d.
(C) AGO1 and SDE3 protein content in mock (–) or P0 induced (+) 7-d-old seedlings. Coomassie blue staining was used as a loading control. "@" indicates hybridization with antibody.
(D) Cartoon depiction of the *sup149.1* mutation, a G-to-A transition in position 1112, in the fourth exon of the *AGO1* coding sequence. This point mutation leads to the replacement of a glycine (GGC) by an aspartic acid (GAC) in position 371 of the AGO1 protein.
See Supplemental File 1 for uncropped source images for immunoblots.

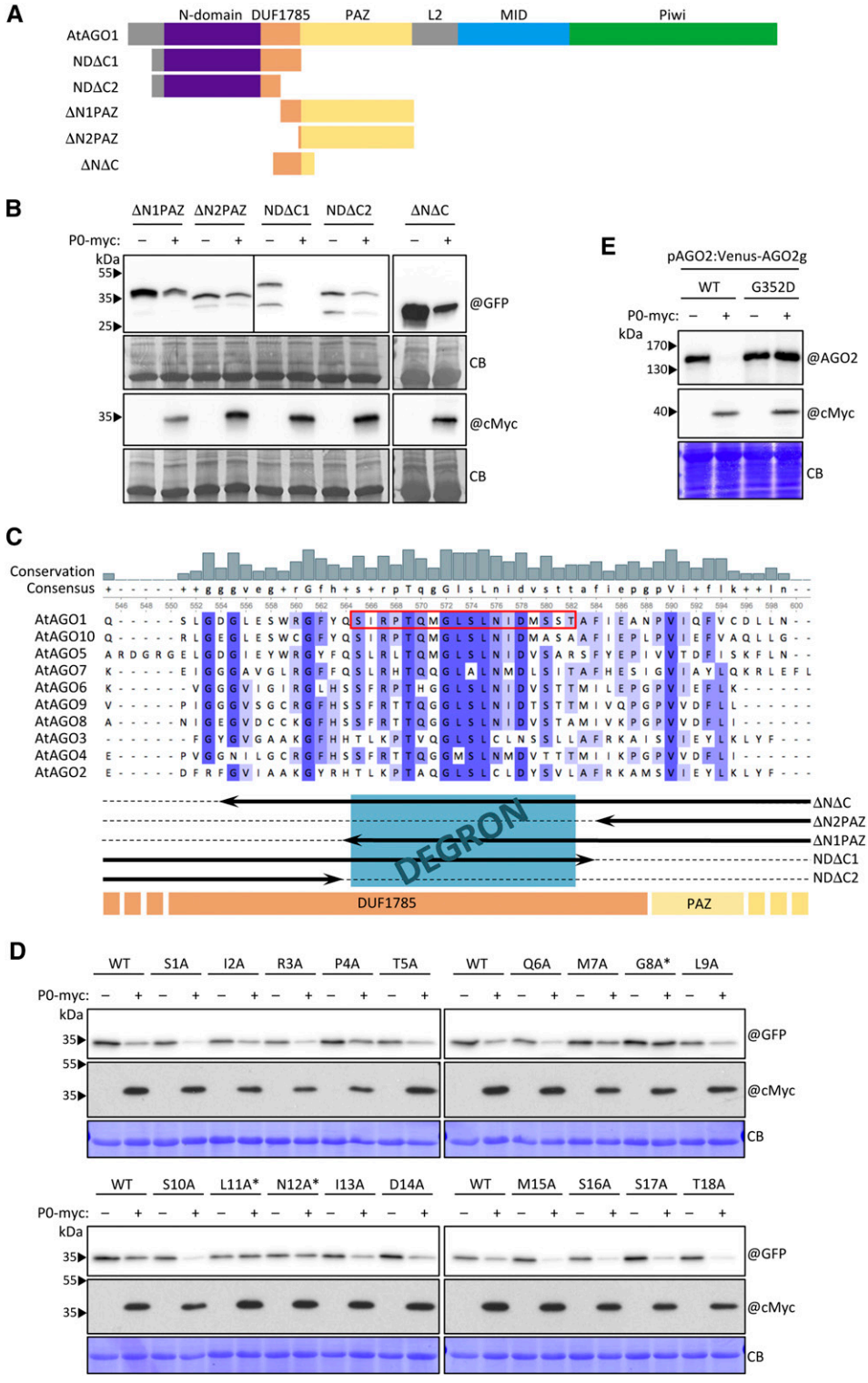

Figure 2. The Conserved DUF1785 of AGO1 Contains the P0 Degron.

(A) Schematic representation of the AGO1 deletion constructs used to assay sensitivity to P0-myc degradation in *N. benthamiana*. Each construct contains a GFP at the C terminus and is under the control of the CaMV 35S promoter. The name of each AGO1 protein domain is indicated on top. PAZ, Piwi-Argonaute-Zwille; L2, Linker 2; MID, middle domain.

(B) Each GFP-AGO1 deletion construct was transiently expressed with (+) or without (–) coinfiltration of the 35S:P0-myc construct. Fusion protein

This sequence conservation likely reflects the importance of this domain for the structure and function of AGO proteins.

Mutation of the DUF1785 Abrogates SCF-Dependant P0 Interaction with AGO1

Next, we investigated if the *ago1-57* mutation alters the physical interaction between P0 and AGO1 in Arabidopsis. Immunoprecipitation (IP) of cMyc-tagged P0 efficiently pulled down the wild-type AGO1 (Figures 3A and 3B) at both 8.5 and 24 h after P0-myc induction. This association was strongly enhanced by MLN4924, a drug that efficiently inhibits CUL1 neddylation and previously shown to impair AGO1 degradation (Derrien et al., 2012). By contrast, the LP1 mutation of P0, in which substitution of the leucine and proline in the minimal F-box motif by two alanine residues abolishes its binding to CUL1 via ASK1/2 adaptor proteins (Pazhouhandeh et al., 2006), abrogated the interaction with AGO1 (Figure 3A). The mutant ago1-27 protein was also efficiently pulled down in similar experiments (Supplemental Figure 2B).

In contrast, the ago1-57 protein was clearly impaired in its capacity to interact with P0-myc, supporting the notion that the degron identified in the DUF1785 is targeted by the viral F-box protein. Moreover, all components of the SCF (CUL1, ASK1, and RBX1) can be equally pulled down by P0-myc in both the wild-type and *ago1-57* backgrounds, indicating that the ability of P0-myc to hijack the E3 ligase was unaltered by the suppressor mutation in AGO1. Together, these results suggest that P0 requires the assembly of an SCF complex to bind AGO1 and that the G371D mutation in the DUF1785 compromises this interaction. Comparative modeling based on the established structure of human AGO2 and other AGOs (Elkayam et al., 2012; Schirle and MacRae, 2012) showed that mutations stabilizing AGO1 in the presence of P0 are not predicted to be on the surface of Arabidopsis AGO1 (Figure 3C; Supplemental Movie 1). This model therefore suggests that the degron is not always accessible, hinting at the existence of a transient, readily attackable conformation of AGO1.

Phenotypic and Molecular Characterization of *ago1-57*

The G371D substitution in *ago1-57* is one of the rare point mutations recovered in the N-terminal part of AGO1 located, moreover, in a hitherto poorly characterized domain of the protein. To characterize the phenotype of the *ago1-57* mutant, plants were grown in soil, alongside several other *ago1* point mutants carrying lesions in different domains of the protein (Figure 3A). Among these alleles, *ago1-38*, the only other mutation recovered in the AGO1 N-terminal part, shows reduced association to membranes (Brodersen et al., 2012) possibly including the endoplasmic reticulum where the AGO1:miRNA RISC mediates translational repression of miRNA target transcripts and at least some level of slicing (Li et al., 2013, 2016). Other mutations tested included *ago1-42* and *ago1-18*, both thought to affect folding of the PAZ domain, and *ago1-49* carrying a lesion in the MID domain structurally important for anchoring the 5′ end of sRNAs (Poulsen et al., 2013). Finally, we also included *ago1-27*, a mutation affecting the PIWI domain of the protein that impairs miRNA-mediated translation repression (Brodersen et al., 2008) but that does not abolish cleavage activity (Li et al., 2016). While *ago1-57* displays clear growth defects compared with the wild-type Arabidopsis reference strain, Col-0 (Figures 4A and 4B; Supplemental Figure 3), it is the mildest of the six *ago1* point mutants compared here. In particular, and despite rosette size differences, *ago1-42*, *ago1-18*, *ago1-49*, and *ago1-27* show a similar aberrant leaf shape not shared with *ago1-57* and *ago1-38*. However, the two latter mutants differ from each other at later stages of their life cycle (Supplemental Figure 3).

RT-qPCR to assay the steady state levels of several known miRNA target transcripts showed that *ago1-27* mutant plants overaccumulated 6 out of 12 targets tested, while none except *ARF10* (*t* test P value <0.01) was deregulated in *ago1-57* (Figure 4C). This suggests that the bulk of miRNA-mediated regulation remains unaffected in *ago1-57*, possibly explaining the mild developmental defects of this mutant. RNA gel blot analysis of the corresponding miRNA species revealed no strong differences in their accumulation compared with Col-0 or *ago1-27* (Figure 4D) and the same was observed for siR255, one of the tasiRNAs originating from the *TAS1* locus. Strikingly, however, passenger strands (also called "star" or "*" strands) of several endogenous sRNA species overaccumulated in *ago1-57* rosettes, flower buds, or both and were particularly evident for miR160c*, miR162*, miR398b*, and miR171a*. However, passenger strand stabilization is not unique to *ago1-57*, as *ago1-27* also displayed elevated levels of some miRNA*, similar to what is observed in

Figure 2. (continued).

levels were assessed by immunoblot using cMyc and GFP antibodies. The @GFP split panel corresponds to the same membrane but with two different exposures. "@" indicates hybridization with antibody.

(C) MUSCLE alignment of Arabidopsis AGO proteins in the DUF1785 region. Amino acid conservation is displayed in blue, the most intense being the most conserved. The 18 amino acids that constitute the P0 degron in AGO1 were defined by boundaries of the degradable versus nondegradable deletion constructs (boxed in red). AGOs identities and deletion constructs depicted by arrows are indicated. Protein domains are highlighted in orange (DUF1785) and yellow (PAZ).

(D) Alanine scanning through the 18 amino acids of the P0 degron. Each residue was mutated to an alanine, in the context of the 35S:ΔNΔC-GFP construct. Each mutant was transiently expressed in *N. benthamiana* with (+) or without (–) coinfiltration of the 35S:P0-myc construct. ΔNΔC-GFP level was assessed by immunoblot using a GFP antibody (@). Asterisks indicate mutations abolishing P0-mediated degradation.

(E) Mutation of the conserved glycine (identified in *ago1-57*) residue in AGO2 is sufficient to block its degradation by P0-myc. The *ago1-57* equivalent (G371D) was introduced in a pAGO2:Venus-AGO2 genomic construct to obtain the G352D construct. Either the wild-type or the mutated Venus-AGO2g construct was transiently expressed with (+) or without (–) coinfiltration of the 35S:P0-myc construct. Levels of the Venus-AGO2 protein were monitored by immunoblot using an AGO2 antibody (@).

See Supplemental File 1 for uncropped source images for immunoblots.

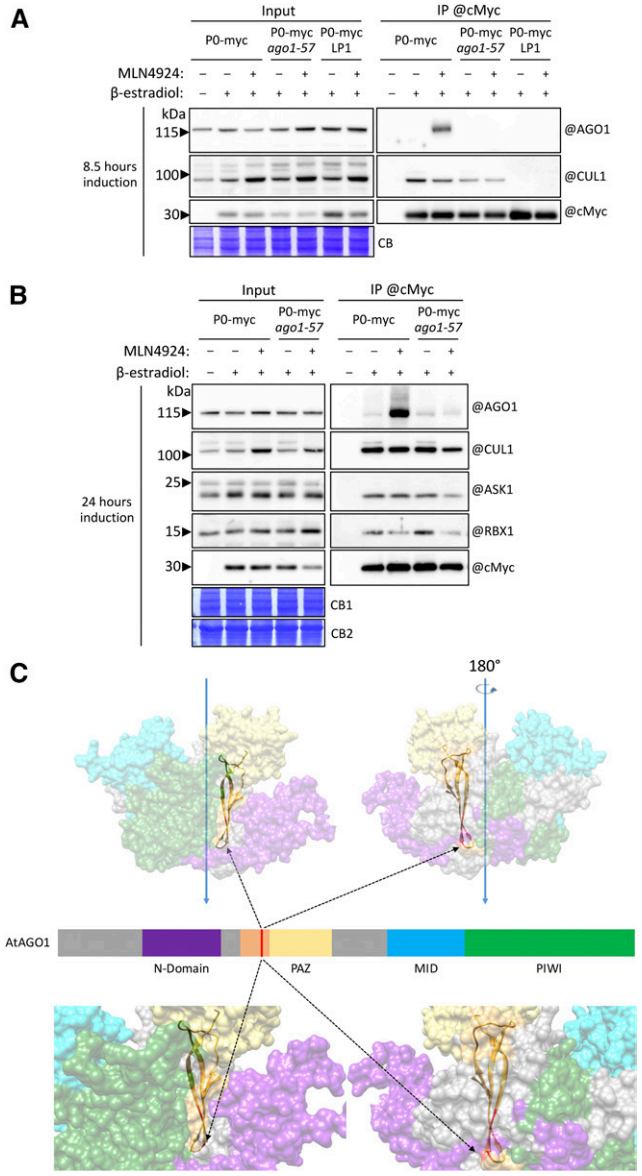

Figure 3. The SCF^{P0} Only Poorly Associates with the ago1-57 Mutant Protein.

(A) Immunoprecipitations of P0-myc were performed on 13-d-old seedlings, cultivated in liquid medium MS + 1% sucrose with either DMSO, 20 μM β-estradiol, or 20 μM β-estradiol + 20 μM MLN4924 for 8.5 h. P0-myc refers to the line containing wild-type AGO1, while P0-myc *ago1-57* contains the point mutant version obtained from the cross. P0-myc LP1 contains two alanines in position 63/64 instead of the minimal F-box motif LP, thereby precluding its association to the SCF. IP experiments demonstrate association of P0-myc with wild-type AGO1, when the neddylation inhibitor MLN4924 is added to the culture. Association is lost with the ago1-57 mutant protein, while the LP1 mutant is neither able to associate with the SCF nor with wild-type AGO1. "@" indicates use of a specific antibody for hybridization or immunoprecipitation.

(B) Immunoprecipitations of P0-myc were performed on 10-d-old seedlings as described in **(A)** for 24 h. Separation was performed on a 4 to 12% acrylamide gradient gel for AGO1, CUL1, and ASK1 blotting (Coomassie blue stain CB1) and on a 15% acrylamide gel for RBX1 and cMyc blotting (Coomassie blue stain CB2). "@" indicates use of a specific antibody for hybridization or immunoprecipitation.

(C) Predictive structural model of Arabidopsis AGO1 based on known structure of eukaryotic AGOs. Domains are color-coded as in Figure 2A. G8 (G371) and L11-N12 of the degron are shown in red in the context of AGO1 structure, and the DUF1785 fold is shown in orange.

See Supplemental File 1 for uncropped source images for immunoblots.

the null *ago1-3* plants in which miR160* and miR173* are stabilized (Arribas-Hernández et al., 2016a). Therefore, this molecular phenotype is shared to various extents among distinct *ago1* alleles linked to point mutations within separate protein domains. Because passenger strand separation is integral to the cognate assembly of mature si/miRNA RISCs, these observations prompted us to investigate this process in more detail with *ago1-57*.

The *ago1-57* Mutation Affects sRNA Duplex Unwinding in Vitro

To address the question of how the *ago1-57* mutation may affect mature RISC assembly, we took advantage of a previously established plant cell free-system (Iki et al., 2010, 2017). The *ago1-57* mutation was introduced into the orthologous FLAG-tagged AGO1 cDNA sequence from tobacco (*Nicotiana tabacum*) by exchanging the conserved G381 residue to Asp. Both the wild-type and mutant forms of FLAG-NtAGO1 proteins were produced by in vitro translation using an extract of evacuolated tobacco BY2 protoplasts (BYL) and incubated with sRNA duplexes (Figure 5A) for which the guide strand was radiolabeled at the 5′ terminus, and the mixture was separated by native gel electrophoresis (Iki et al., 2010, 2017).

As expected, single-stranded products were detected only in the presence of Flag-NtAGO1 (Figure 5B) and indicate mature RISC formation. When Flag-NtAGO1$^{ago1\text{-}57}$ was used, single-stranded RNA (ssRNA) products were barely visible, except for miR173, which showed wild-type level of ssRNA accumulation. Unlike most Arabidopsis miRNAs, which are 21 nucleotides in size, miR173 occurs naturally as a 22-nucleotide species in vivo. We thus tested if the presence of an additional nucleotide was sufficient to overcome the RISC assembly defects of Flag-NtAGO1$^{ago1\text{-}57}$. However, assaying a synthetic GFP-derived siRNA duplex of 22 nucleotides (siR22) yielded the same inability to form the ssRNA product.

To discriminate between defective loading and defective duplex unwinding of Flag-NtAGO1$^{ago1\text{-}57}$, Flag-NtAGO1 was immunoprecipitated on anti-Flag resin. Resolving of the sRNA species bound to Flag-NtAGO1 showed that wild-type NtAGO1 mostly contains the ssRNA form of the considered sRNA. By contrast, Flag-NtAGO1$^{ago1\text{-}57}$ loaded the dsRNA product, yet the ssRNA product remained well below the levels observed for Flag-NtAGO1 (Figure 5C). The only exception was for miR173, which formed ssRNA product at a level comparable to Flag-NtAGO1. From these data, we conclude that the *ago1-57* mutation does not affect dsRNA duplex binding to AGO1, but impairs and/or delays the process of unwinding leading, presumably, to stalled forms of AGO1 still bound to dsRNA. Overall, our data are consistent

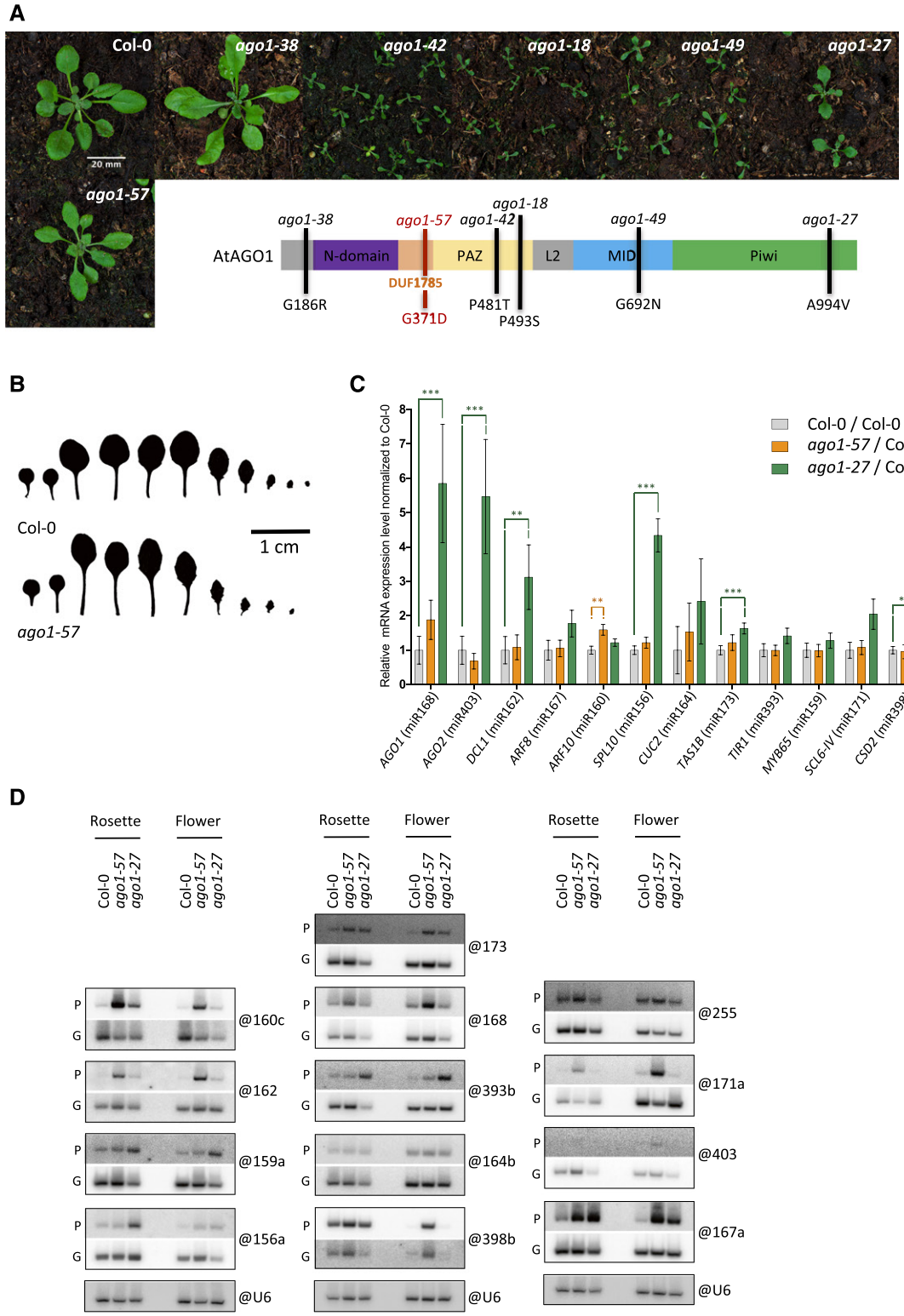

Figure 4. Phenotypic and Molecular Characterization of the *ago1-57* Mutant.

(A) Top panel: Representative mutant plants, grown on soil for 32 d. Bottom panel: Schematic AGO1 sequence represents names, positions, and mutated amino acids of selected mutants; *ago1-57* is represented in red.
(B) Leaf series of Col-0 and *ago1-57* 21-d-old plants. Leaves are arranged from left to right in order of emergence.

with the work of Kwak and Tomari (2012) showing that the N domain of human AGO2, including the DUF1785, is necessary for duplex unwinding of siRNA and miRNA duplexes during RISC assembly. However, a later study using transfected mouse embryonic fibroblast cells with AGO2 mutants and short hairpins suggests the N domain is not essential for this molecular event (Gu et al., 2012), since a PAZ mutation combined with a catalytic site mutation abolished unwinding of miRNA-like duplex, which was not the case with a N domain-slicer deficient mutant that retained its ability to unwind the same duplex. It is therefore important to characterize the effect of the DUF1785 on miRISC and siRISC formation in the context of a whole organism.

The *ago1-57* Mutation Leads to in Vivo Retention of sRNA Duplex into AGO1

We next investigated the impact of the *ago1-57* mutation on the Arabidopsis total sRNA landscape by conducting comparative deep-sequencing analyses in the *ago1-57* versus Col-0 backgrounds. We also immunoprecipitated endogenous AGO1 in both backgrounds and conducted deep-sequencing analysis of the sRNA bound to either wild-type AGO1 or ago1-57 (Supplemental Figure 4A). A genome-wide profiling of deregulated loci revealed that 57 and 227 genomic loci over- and underaccumulated sRNAs, respectively, in *ago1-57* compared with Col-0 total sRNA libraries (Figures 6A and 6B). Among those, about a third consisted of annotated *MIR* genes (34.4% down $n = 78$ and 29.8% up $n = 17$) (Supplemental Figure 4B). In the AGO1 versus ago1-57 IPs, a similar number of genes presented significant increase or decrease in sRNA accumulation, amounting to approximately half of the loci identified in total sRNA libraries (Figure 6B). All *MIR* genes displaying enhanced sRNA levels in the ago1-57 IPs (21.6% increased, $n = 41$; 25.8% decreased, $n = 31$; Supplemental Figure 4C) encompassed those found in total sRNA libraries, with only one exception (Supplemental Figure 4D). Thus, the prolonged steady state of miRNAs bound to ago1-57 could explain their overaccumulation in the total sRNA fraction.

Since ago1-57 was found to stack dsRNA duplexes in vitro, it was likely that at least part of the overaccumulated miR products were, in fact, passenger strands. We therefore separated reads mapping to either the 5p or the 3p from all *MIR* loci previously annotated as duplex in miRBase v21 (Supplemental Figure 4E). This revealed that 47 miRNAs enriched in the wild type were exclusively depleted in *ago1-57* and that 13 miRNAs depleted in the wild type were enriched in *ago1-57*. Conversely, 45 miRNAs displayed elevated levels in ago1-57 IPs while 27 displayed reduced levels when compared with AGO1 IPs (Supplemental Figure 4E). Since the identified mature miRNA products were not annotated as either guide or passenger strand, we calculated the absolute ratio between 5p and 3p products ($-1 \times \log_e[5p/3p]$) and represented the results as a box plot in which proximity to 0 suggests existence as a duplex (Figure 6C). In wild-type samples, a comparison between total and IP libraries showed that AGO1-bound miRNAs tend to accumulate as single strands as expected from bona fide cargoes of a mature AGO1:miRNA RISC. By contrast, total miRNAs are mostly detected as duplexes, suggesting that not all miRNA duplexes produced in vivo are loaded and unwound in AGO1. Interestingly, this ratio was skewed in the mutated AGO1 in libraries prepared from *ago1-57*. This was particularly striking in the IPs in which duplexed sRNA retention was observed, in agreement with the in vitro results (Figure 5).

To further validate these genome-wide observations, we performed additional AGO1 IPs in seedlings of wild-type plants versus *ago1-27* and *ago1-38*, since these two mutant alleles display rosette sizes comparable to those of *ago1-57* and Col-0, and retain detectable amount of AGO1 (Figure 6D, bottom panel). RNA gel blot analysis revealed that miRNA* tends to overaccumulate in the total RNA fraction of the *ago1* mutants (Figure 6D, top panel). This was most apparent for miR160c*, which, unlike other miRNA passenger strands, is detectable in the wild-type background and strongly stabilized in *ago1-57*, *ago1-27*, and *ago1-38*. Consistent with the IP RNA-seq data, *ago1-57* retained all tested miRNA* and siRNA255* species, accompanied by slight decrease in the corresponding guide strand. Notably, the main 21-nucleotide products seen in *ago1-57* IPs were accompanied by one or several faster migrating products, suggesting trimming of the stacked products. Intriguingly, *ago1-38* overaccumulated miR171a* and siR255* to the same extent as *ago1-57* in the total sRNA fraction, but also simultaneously stacked miR171a* inside AGO1, but none of the other passenger strands tested. Separating the RNA recovered from the IP on a native gel acrylamide, after labeling of their 5′ extremities (Figure 6E), showed a situation reminiscent of what is observed in the cell-free system (Figure 5C). While the wild-type AGO1 mostly contains single-stranded sRNA species as well as a detectable amount of double-stranded species, the double-stranded species were

Figure 4. (continued).

(C) RT-qPCR analysis of representative AGO1-miRNA target mRNA in Col-0 (gray), *ago1-57* (orange), and *ago1-27* (green). Total RNA samples were extracted from 5-week-old rosettes grown on soil and RT-qPCR was conducted on four individual biological replicates for each genotype. Expression levels are shown relative to Col-0 for the two mutants. For each target, the relevant miRNA is indicated in brackets. Compared to *ago1-27*, *ago1-57* displays very little change in target mRNA levels. A *t* test was performed to compare both mutant genotypes to Col-0. Significant differences in RNA abundance are displayed above each pairwise combination. ***$P < 0.001$ and **$P < 0.01$.

(D) RNA gel blot analysis of the steady state accumulation of corresponding miRNAs from **(C)** and siRNA255 originating from the *TAS1* locus. Rosette and flower tissues were used for this analysis and simultaneously blotted on three separate membranes probed independently, each stripped and reprobed several times. For the RNA gel blot analysis conducted on rosettes, equal amounts of RNA from the four biological replicates were mixed and 40 μg was loaded on a gel for each genotype. Each miRNA is indicated on the right side of the image. P, passenger strand; G, guide strand. While guide strand accumulation remains mostly unaffected, *ago1-57* typically shows overaccumulation of most passenger strand miRNA. "@" indicates hybridization with the indicated DNA probe.

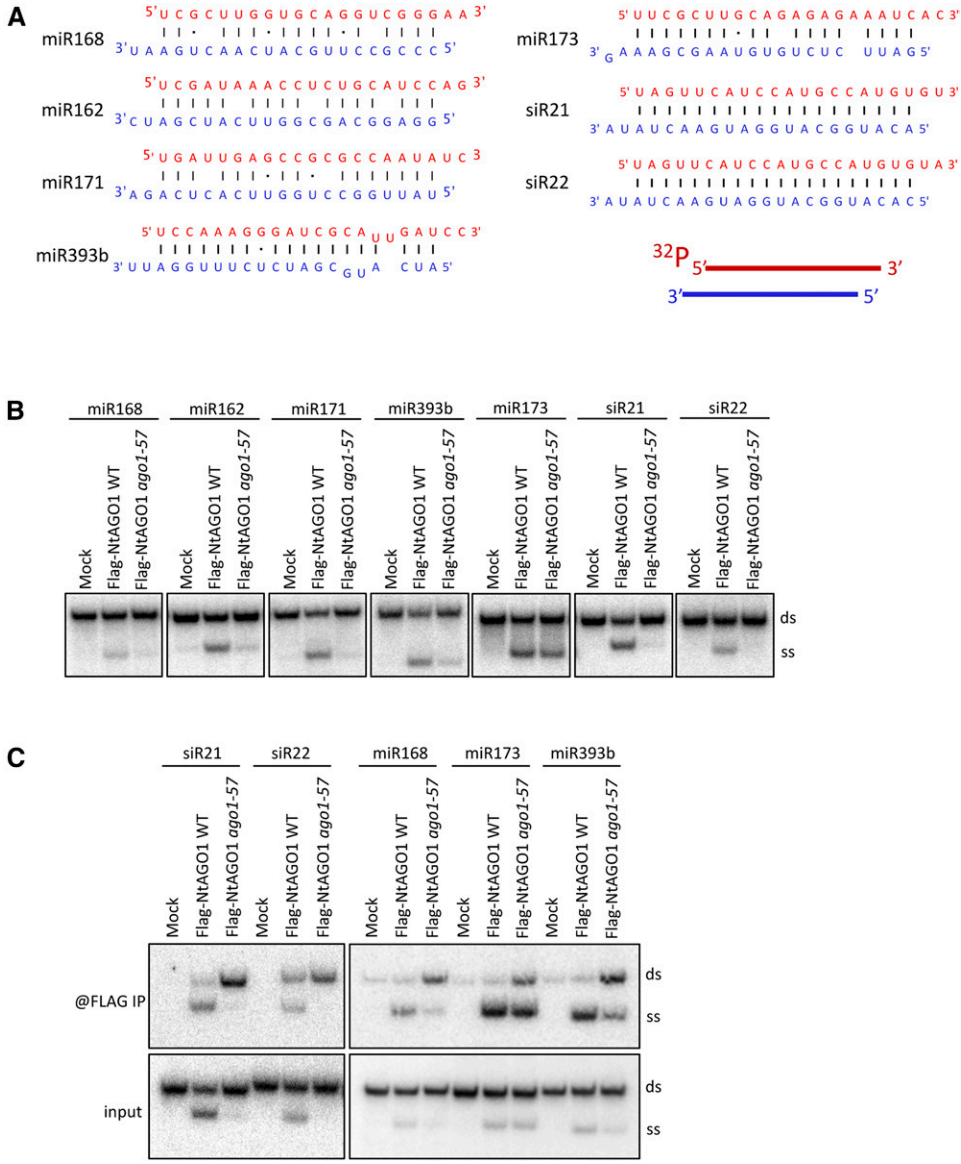

Figure 5. The *ago1-57* Mutation Induces Stacking of sRNA Duplexes inside AGO1 during RISC Formation.

(A) Small RNA duplex sequences used in **(B)** and **(C)**. Sequence of the mature miRNA is shown in red in 5′→3′ orientation, while the paired passenger strand is depicted in blue. Paired nucleotides are joined by a bar and wobble paired nucleotides by a dot. In these assays, the guide strand (red) is ^{32}P labeled at the 5′ extremity and annealed to the cold passenger (blue) strand.

(B) Effect of the *ago1-57* point mutation on the generation of single-stranded (ss) guide sRNAs, in the cell-free RISC formation system using evacuolated BY2 extracts (BYL). Either wild-type NtAGO1 or the ago1-57-equivalent mutant was expressed in BYL by in vitro translation and incubated for 30 min with indicated sRNA duplexes containing ^{32}P-labeled guide strands. Resultant RNAs were extracted and analyzed on native acrylamide gel, allowing differentiation between residual substrate double-stranded (ds) and processed single-stranded sRNA. Mock refers to a BYL extract with labeled sRNA but without NtAGO1. This assay was repeated for several miRNA duplexes as well as two identical siRNA perfect match duplexes, differing only in size by one added nucleotide. The *ago1-57* mutation impairs accumulation of several single stranded miRNA, but also of the tested siRNAs, regardless of their size

(C) Effect of the *ago1-57* point mutation in the removal of the passenger strand from the sRNA duplexes. Experiment was performed as described in **(B)**, and Flag-tagged NtAGO1 was further purified with @Flag antibodies. Total (input) or AGO1-bound RNA (@Flag-IP) was analyzed by native acrylamide gel electrophoresis. The *ago1-57* mutation induces retention of duplexed sRNA inside AGO1 to varying degree, thereby decreasing the generation of single-stranded sRNAs loaded into RISC.

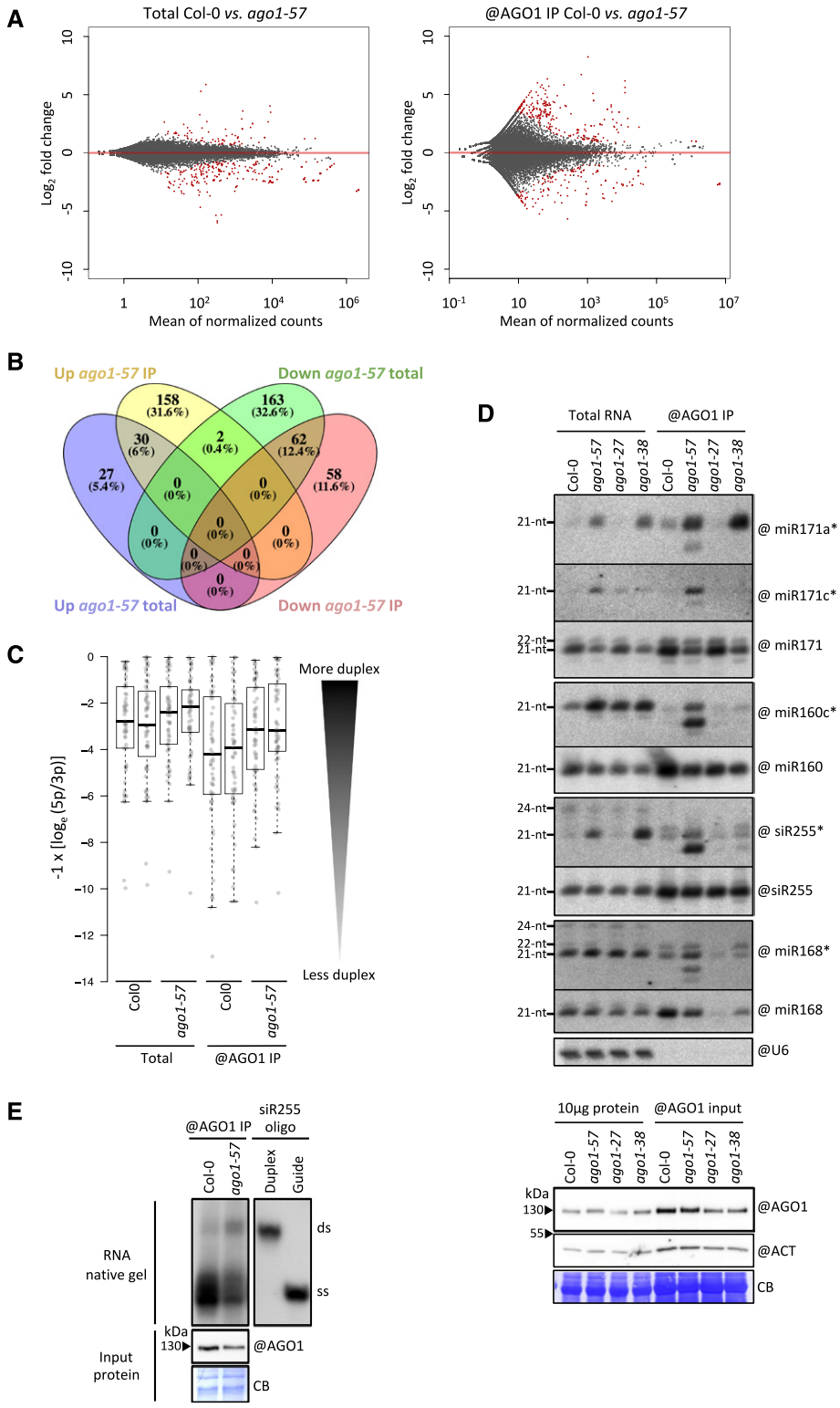

Figure 6. In Vivo Analysis of sRNA Accumulation in the *ago1-57* Mutant.

(A) Differential analysis of Col-0 normalized sRNA reads (JBT17-18 and JBT23-24) compared with *ago1-57* normalized sRNA reads (JBT19-20 and JBT25-26). Left panel: Normalized total RNA libraries. Right panel: Normalized @AGO1 IP libraries. Abundance (mean of normalized counts) is displayed on the horizontal axis and $\log_2$ fold change on the vertical axis. Loci with an adjusted P value lower than 0.05 are highlighted in red.

clearly more abundant in ago1-57, and the single-stranded ones less abundant. From these combined results, we conclude that *ago1-57* uniquely stacks passenger strands into AGO1, a feature not shared with other *ago1* missense alleles.

The *ago1-57* Mutation Affects PhasiRNA Production and Fully Suppresses S-PTGS

One striking result from the differential analysis of sRNA accumulation in the *ago1-57* mutant compared with Col-0, was the significant reduction in secondary sRNAs spawned from 132 protein-coding gene loci including 27 pentatricopeptide repeat genes (*PPRs*), three nucleotide binding site-leucine-rich repeat genes (*NBS-LRRs*), four auxin-related genes (auxin response factors and auxin signaling genes), *AGO1*, and bHLH-encoding genes (Supplemental Data Set 1A), most of which were previously described as phasiRNA-producing loci (Howell et al., 2007; Li et al., 2016). *PPR* genes strongly contribute to the bulk of Arabidopsis phasiRNA (Chen et al., 2007; Howell et al., 2007) and most of these loci (from the *PPR-P* clade) are encoded at two distinct regions on chromosome 1. Upon their targeting by miR161 and miR400, as well as by several tasiRNA produced from the TAS2 gene, the PPR transcripts are converted into ds-RNA by RDR6/SGS3 to generate abundant phasiRNAs (Chen et al., 2007). All considered, the annotated phasiRNA-producing genes represent approximately one-third of all the genes showing a reduced sRNA abundance in *ago1-57*.

While production of phasiRNA from protein-coding loci seems to be specifically impaired, in the *ago1-57* mutant, this was not the case for tasiRNAs produced from noncoding transcripts. Indeed, only three out of eight *TAS* genes (*TAS1c*, *TAS2*, and *TAS3b*) displayed a mild reduction in the levels of their associated sRNAs (Figure 7A; Supplemental Data Set 1A). Accordingly, miR173, the trigger for *TAS1*- and *TAS2*-dependent tasiRNA production, is one of the less affected miRNAs in terms of duplex unwinding in *ago1-57* (Figure 5). This loss of phasiRNA but not tasiRNA production is reminiscent of the effect of AGO1 slicer-deficient mutants (Arribas-Hernández et al., 2016b) except that tasiRNAs phasing within a dominant sequence register is also lost in the latter, but maintained in *ago1-57* (Figure 7B; Supplemental Figure 5).

To understand the loss-of-phasiRNA production in *ago1-57*, we analyzed the sRNAs triggering their production from *PPR* transcripts. Since miR161.1 and miR161.2 are not affected in the *ago1-57* mutant, we analyzed tasiR2140 [TAS2-3′D6(–)], a product of the *TAS2* mRNA and essential for the production of phasiRNA from the *PPR-P* gene clade (Chen et al., 2007; Howell et al., 2007; Arribas-Hernández et al., 2016b). This analysis revealed that the most abundant tasiR2140 species is a 22-mer harboring a 5′ U nucleotide. While accumulation of this tasiRNA is not affected in the *ago1-57* mutant, its passenger strand is stabilized in ago1-57 IPs (Figure 7C).

Incidentally, the $\log_{10}$ ratio of the guide versus passenger strand of this siRNA is significantly reduced in *ago1-57* mutant, both in total and IP samples (Figure 7D). The tasiRNA2140 duplex is therefore likely poorly unwound, and its stacking into AGO1 might alter efficient activation of the tasiRNA2140-programmed RISC, explaining the strong impairment of *PPR-P* genes silencing, identical or stronger than that of *ago1-27* (Figure 7E), despite its otherwise modest effect on miRNA target transcripts (Figure 4C).

Collectively, these results suggest that the *ago1-57* effects are exacerbated when AGO1 is loaded with perfect duplexes such as those formed by siRNAs. Under such conditions, the duplex would be too stable to be efficiently unwound by ago1-57, leading to impaired silencing of the corresponding target. Consistent with this interpretation, *ago1-57* abolishes the silencing of the p35S:GUS transgene of line L1, in which multiple rounds

Figure 6. (continued).

(B) Venn diagram depicting overlap between sRNA generating loci that are either enriched or depleted in *ago1-57* compared with the wild type, in total and @AGO1 IPs. See Supplemental Data Set 1 for corresponding loci and sRNA count.

(C) Box plot representation of accumulation of sRNA reads over miRNA 5p and 3p annotations. The vertical axis represents the absolute value of the $\log_e$ 5p/3p ratio multiplied by –1, while library identities are indicated below the box plot. Only miRNAs with at least 100 reads overlapping the 5p or the 3p in at least one library were considered (n = 63 out of the 93 miRNA precursors with both 5p and 3p annotation in miRBase V21). In order to avoid division by 0, read count values were transformed into pseudo-counts by adding 1 to all values. The closer the box plot is to 0 the more miRNA 5p and 3p annotations have similar amounts of overlapping reads.

(D) In vivo analysis of accumulation of diverse sRNAs in Col-0 and three *ago1* point mutants, in total RNA and AGO1 immunoprecipitates. *ago1-38* and *ago1-27* were used, as they presented moderate growth defects and similar protein accumulation to Col-0 and *ago1-57*, and were therefore comparable. Top panel: @AGO1 IP was performed from 18-d-old seedlings to document accumulation of AGO1-bound sRNA. Both total RNA and RNA recovered in the IP were extracted. Both *ago1-57* and *ago1-38* appear to accumulate passenger small RNA in the total RNA fraction, for several of the considered loci. On the other hand, *ago1-57* retains star strand inside the in vivo AGO1 RISC complex for all considered loci. The *ago1-57* mutant also displays products below 21 nucleotides. Bottom panel: AGO1 protein level from both total extracted and IP buffer-extracted proteins, shown as an estimate of the amount of AGO1 that could be immunoprecipitated. "@" indicates hybridization with the indicated DNA probe, or use of a specific antibody for immunoprecipitation. See Supplemental File 1 for uncropped source images for immunoblots.

(E) Native In vivo analysis of RNA species found in the AGO1 IP (@) separated on a native acrylamide gel. Top panel: RNA was recovered from AGO1 IPs performed on 11-d-old seedlings, and ^{32}P labeled at the 5′ extremity. Resultant RNAs were analyzed on native acrylamide gel, allowing differentiation between double-stranded (ds) and processed single-stranded (ss) sRNA. Synthetic siR255/siR255* was used as a size control, either for double-stranded species (annealed and nondenatured) or single-stranded species (heat-treated before loading). The ago1-57 protein contains more global double-stranded species and less single-stranded species then the wild-type AGO1. Bottom panel: AGO1 protein level from IP buffer-extracted proteins, shown as an estimate of the amount of AGO1 that could be immunoprecipitated. "@" indicates hybridization with the AGO1 specific antibody or use of the same antibody for immunoprecipitation.

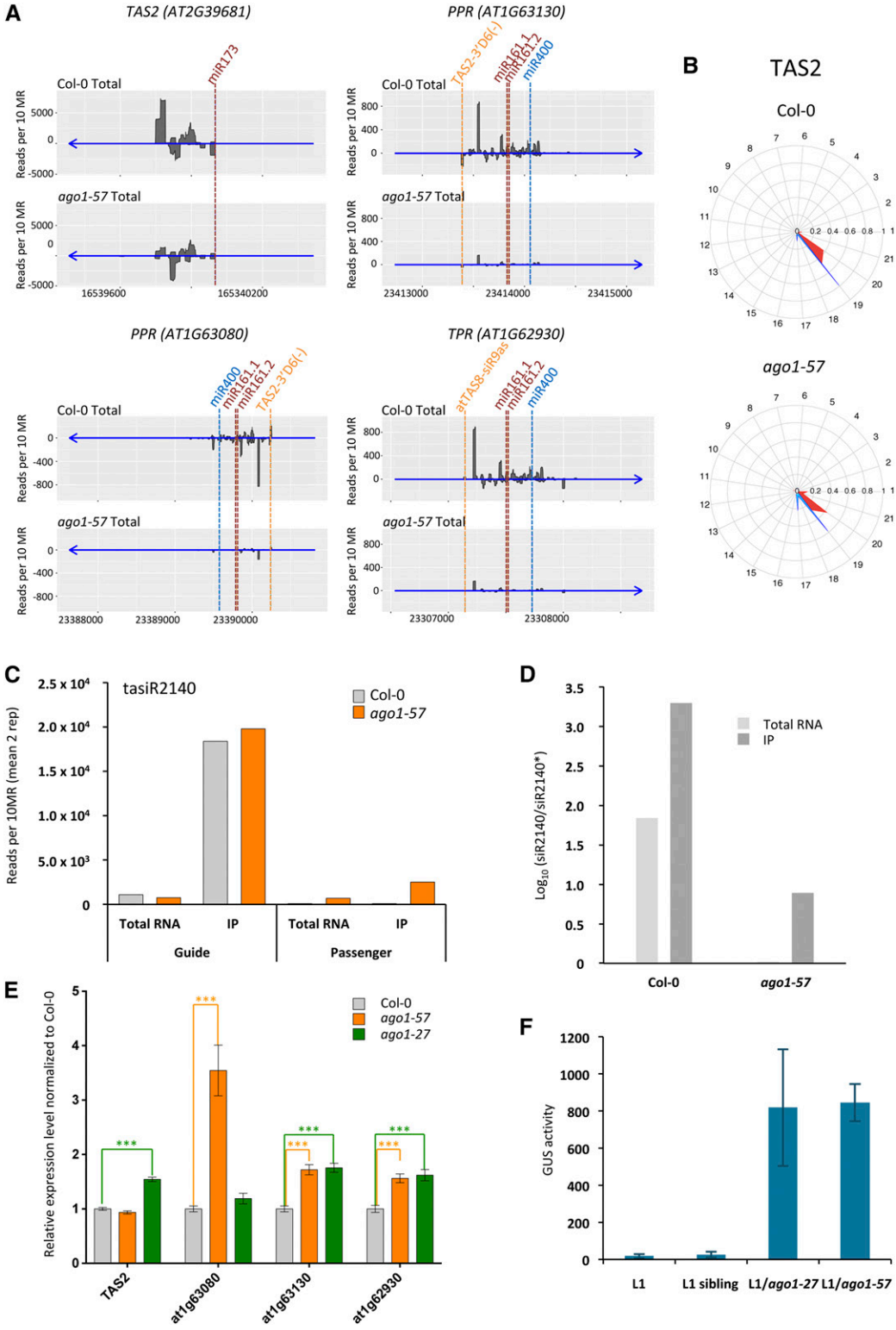

Figure 7. The *ago1-57* Mutation Impairs Secondary sRNA Production, Except for tasiRNAs.

(A) Mapping of sRNA reads on *TAS2* and three *PPR* genes (At1g63080, At1g63130, and At1g62930) targeted by the *TAS2*-derived tasiRNA: tasiR2140 [also named TAS2-3′D6(–)]. Positions of known small RNA triggers are indicated by dashed lines

(B) Phasing of sRNAs over the *TAS2* transcript in Col-0 and *ago1-57*.

of AGO1/SGS3/RDR6/DCL2/4-mediated amplification are required to complete S-PTGS (Parent et al., 2015; Figure 7F).

DISCUSSION

SCF^{P0} E3 Ligase Recognizes a Conserved Degron in AGO Proteins

The polerovirus VSR P0 encodes an F-box protein that hijacks the host SCF-type E3 ubiquitin ligase to promote degradation of the central miRNA-RISC component AGO1 (Baumberger et al., 2007; Bortolamiol et al., 2007; Csorba et al., 2010). Here, we have provided novel insights into the mechanism of AGO1 recognition by the SCF^{P0} complex. Using both forward genetics and serial-deletion analyses we identified key residues in the AGO1 protein, which are required for P0-mediated degradation and an 18-amino acid peptide containing these residues was sufficient to confer P0-dependent degradation to the GFP reporter protein and therefore fulfils the criterion of a "degron" (Varshavsky, 1991). This sequence, and in particular the G371 residue, is conserved in most plant AGO proteins, suggesting that they are all potential substrates of the SCF^{P0} E3 ubiquitin ligase. Indeed, we could show that P0 not only mediates AGO1 turnover, but also triggers the degradation of endogenous Arabidopsis AGO2 and AGO4, while an *ago1-57* equivalent mutation in the G352 of AGO2 fully stabilizes the protein in presence of P0 (Figure 2E). At present, it is still unclear how the F-box protein P0 interacts with the identified AGO1 degron, and we cannot exclude the possibility that this interaction also involves a specific posttranslational modification and/or requirement for an additional factor. Notably, P0 proteins from different viruses lack sequence similarities and no defined structure or protein domain could be predicted, though most of them are able to mediate the decay of AGOs (Fusaro et al., 2012; Almasi et al., 2015; Cascardo et al., 2015). Because mutation of the P0 F-box motif impaired the interaction with AGO1 (Figure 3A), it is likely that P0 is folded to recognize AGOs only in the context of an assembled SCF. Because our genetic screen also identified four missense alleles of P0 that fully suppressed AGO1 degradation without affecting the F-box motif (Supplemental Figure 1), pursuing studies of these mutants by assessing their ability to bind the SCF and AGO1 might provide important further clues.

Interestingly, homology modeling of Arabidopsis AGO1 protein according to the structure of human AGO2 (Elkayam et al., 2012; Schirle and MacRae, 2012) indicates that the degron is not directly accessible on the protein's surface (Figure 3C; Supplemental Movie 1). Nevertheless, all established AGO structures have been obtained from sRNA-bound AGOs, therefore restricting the ability to model an unloaded AGO1. Structural and other studies have further hinted at the probably flexible AGO domain organization, likely explaining the difficulty to crystallize RNA-free form of AGOs. These studies also showed that binary-to-ternary complex transition (during association to the target RNA) leads to rotation of both protein lobes, and particularly of the ND and PAZ domains (Wang et al., 2008, 2009). It has been proposed that P0 acts upstream of AGO1 loading (Csorba et al., 2010) as P0 is very effective in degrading newly synthesized AGO1 after transient expression in tobacco leaves, but not the endogenous, preassembled AGO1 complex. Elimination of the unloaded form of AGOs by viruses is expected to efficiently suppress anti-viral RNAi by preventing the neo-formation of viral siRNA-RISC. These collated observations favor a model in which the wild-type degron is primarily exposed to the SCF^{P0} before loading, and in which the mutated glycine leads to compromised degron recognition, either by loss of direct recognition or by reduced rate of AGO1 association to an accessory factor/modified residue normally recognized by P0. Once the active process of loading, which is facilitated by HSP90 and fueled by ATP, has begun, AGO1 conformational changes, including by rotation of the N-terminal part of the protein, could thus result in concealment of the degron from the SCF^{P0}.

Function of the DUF1785 in sRNA Duplex Unwinding

In contrast to the PAZ, MID, and PIWI domains for which multiple mutant alleles of AGO1 have been identified (Poulsen et al., 2013), only one mutation (*ago1-38*) was reported in the N-terminal part of the protein (Brodersen et al., 2012). This mutation was shown to affect the association of AGO1 to membranes, though it is currently unknown how AGO1 activity is affected.

In metazoans and to a lesser extent in plants, the different steps of RISC assembly have been well described. Typically, the process starts by the loading of a sRNA duplex, either as a perfectly matched siRNA duplex or as a mismatch-containing miRNA/miRNA* duplex. This process relies on ATP hydrolysis and requires chaperoning, presumably to induce conformational changes in AGO that favor the directional entry of the duplex (Kawamata et al., 2009; Iki et al., 2010; Iwasaki et al., 2010; Yoda et al., 2010; Ye et al., 2012). Polarity of the duplex entry is of paramount importance, since the proper strand has to be selected as guide. This is achieved by sensing the relative thermodynamic stability of both ends of the duplex, either with the help of other components or by the AGO protein itself (Liu et al., 2003; Tomari et al., 2004; Eamens et al., 2009; Okamura et al., 2009; Iwasaki et al., 2015). As a result, the 5′ end of the guide strand is anchored by the MID/PIWI pocket conserved inside AGO, while the passenger strand is not directly bound to AGO. The subsequent steps comprise the opening of the duplex starting from

Figure 7. (continued).

(C) Abundance of tasiR2140 guide strand and passenger strand in Col-0 seedlings compared with *ago1-57*, in total RNA and @AGO1 IP.

(D) Comparison of the $\log_{10}$ guide/passenger ratio in Col-0 and *ago1-57*, calculated for both total RNA and AGO1-IP RNA samples.

(E) Comparison of *TAS2*, At1g63080, At1g63130, and At1g62930 mRNA accumulation in Col-0, *ago1-57*, and *ago1-27* seedlings. Total RNA was extracted from 2-week-old seedlings. A *t* test was performed to compare mutants to Col-0. Significant differences in RNA abundance are displayed above each pairwise combination. ***$P < 0.001$ and ** $P < 0.01$.

(F) Comparison of the GUS activity measured in L1, L1/*ago1-57*, and L1/*ago1-27* lines.

the 3′ end of the guide, an action termed "wedging," anchoring of this 3′ extremity in the PAZ domain (Elkayam et al., 2012) and ultimately ejection of the passenger strand or "unwinding," to form the mature RISC programmed with a sRNA. While cleavage of the passenger strand facilitates its removal from AGO when loaded with siRNA duplexes (Matranga et al., 2005; Leuschner et al., 2006), the N-terminal part of the protein, including the DUF1785, seems to be the main driving force during this process (Kwak and Tomari, 2012; Park and Shin, 2015). However, a later study using transfected mouse embryonic fibroblast cells with AGO2 mutant, rather implicated the PAZ domain in unwinding of miRNA-like duplex (Gu et al., 2012).

Our results extend these previous studies and clearly define the DUF1785 as an important actor of RNA duplex unwinding. This conclusion is supported by several observations: First, in a cell-free in vitro assay, the prominent form of sRNA found in the immunoprecipitated AGO1 mutant were duplexes, with minimal amount of single-stranded guide (Figure 5), indicating that the mutant retains its ability to load duplexes, but loses the ability to then separate both strands of the duplex, to a varying degree depending on the considered duplex. Second, in vivo IP experiments clearly demonstrated that a population of miRNA* is loaded into the mutant AGO1 (Figure 6), reflecting their probable stabilization at the duplex stage, a situation not seen in the wild type, where the passenger strand is ejected and presumably quickly degraded. While we cannot exclude that, in vivo, ago1-57 loads the passenger instead of the guide, giving rise to improperly programmed miRNA*-RISCs, we do not favor this hypothesis, since polarity of the duplex is decided during the loading step (see above) and would lead to a decrease in miRNA target silencing, accompanied with morphological defects much closer to that of severe *ago1* alleles, which is not the case (Figure 4A; Supplemental Figure 3). Therefore, the DUF1785 as well as the ND likely pivot together to allow rapid processing of the passenger strand, enabling efficient transitioning to a mature RISC

According to the existing data, it is unlikely that the unwinding defect of ago1-57 is a direct consequence of a slicing defect: In particular, the proper phase was conserved for all concerned tasiRNA generating loci (Figure 7B; Supplemental Figure 5), a feature not shared with catalytically dead AGO1 in which phasing rather than production is impaired (Arribas-Hernández et al., 2016b). Also, phenotypes of plants containing catalytically dead AGO1 show very severe developmental defects linked with their disability to process their mRNA targets (Arribas-Hernández et al., 2016a), phenotypes that are not observed for *ago1-57*. Thus, ago1-57 likely sustains normal cleavage activity of target mRNA (Figure 4C), while on the other hand, the PIWI domain in the ago1-57 conformation seems unable to properly cleave the passenger strand during unwinding. Indeed, the intact, rather than processed, sRNA duplexes were bound to ago1-57 (Figure 5C), suggesting a slicing defect only during RISC formation. Thus, this observation implies the existence of two separate modes of slicing for AGO1 and is supported by the previous demonstration that slicer-deficient mutants are also unable to unwind tasiRNA* species, but not miRNA*, presumably because slicer activity is only mandatory for perfect strand separation (Iki et al., 2010). Overall, this data collectively support a model in which movement of the N-terminal lobe during wedging entails movement of the PIWI to a position favorable to passenger strand cleavage, compromised in the *ago1-57* mutant. Such domain rearrangement is required for slicing-dependent, and possibly -independent unwinding, but is dispensable during target mRNA slicing.

An additional question arising from our observations pertains to the identity of the affected miRNA/miRNA* in *ago1-57*. Why are some specific duplexes affected and not others? One likely explanation would be that affected duplexes possess stronger thermodynamic stability than the ones undergoing unwinding in *ago1-57*, especially on the 3′ extremity of the duplex. Although we could not distinguish any particular feature of the affected duplexes, we could still observe a strong bias for the perfectly matched siRNA duplexes, fully retained inside AGO1 as duplexes in the in vitro pull-down experiment, while this was not the case for the tested miRNAs (Figure 5C). Hence, siR2140* was stacked strongly enough to lead to near total loss of the downstream phasiRNA (Figure 7D). Finally, *ago1-57* was unable to silence the L1 line, in which sense GUS transgene silencing heavily relies on the amplification step performed by AGO1, RDR6, SGS3, and DCL2/4 (Parent et al., 2015) (Figure 7F). These observations suggest that *ago1-57* cannot induce slicer-dependent unwinding of perfectly matched duplexes such as siRNAs, while it is markedly less affected once bulges and mismatches are present in the duplex to allow the slicer-independent unwinding, as it is the case for miRNAs.

While the stacking of passenger strands inside AGO1 seems to be a hallmark of *ago1-57*, overaccumulation of duplexes in the total sRNA fraction was also observed in *ago1-27* and *ago1-38* for a range of miRNA* (Figures 4D and 6D). This is similar to what is observed in the null *ago1-3* plants in which miR160* and miR173* are stabilized (Arribas-Hernández et al., 2016a). Although we have not similarly assayed other alleles, the broadness of the effect suggests a loading defect common to many AGO1 mutant proteins, but varying in range. This common effect could be due to structural constrains imposed on the protein by mutations, leading to a structure less fit for duplex entry or for cochaperone association. In such a scenario, methylated sRNA duplexes would exist as a reservoir for several competing AGO molecules, the latter being the rate-limiting factors of the association reaction, and this effect would be amplified in defective AGOs. This could in turn partly explain why P19 is able to access miRNA duplexes instead of AGO1 (Chapman et al., 2004). Additionally, at least some passenger strand species could appear to be stabilized by spurious loading into other AGOs that could select the passenger over the guide strand, due to a different 5′ preference, as it is the case for miR393* into AGO2 (Zhang et al., 2011) and miR390a* in AGO5 (Mi et al., 2008).

Finally, our study uncovers an unexpected aspect of sRNA processing. Indeed, we typically observe signals corresponding to a smaller version of blotted passenger strands in ago1-57 IP, but never on the guide strand (Figure 6D). This may suggest trimming of the passenger strand extremities, although signature reads for such trimming products were not recovered in the IP libraries, thereby precluding addressing the question of their size as well as the orientation of the trimming. Absence of these species in the libraries suggests that they did not display either the 5′ monophosphate or the 3′ hydroxyl required

for adaptor ligation. To our knowledge, only 3′ trimming and 3′ uridylation on AGO1 bound guide miRNAs is described (Ramachandran and Chen, 2008; Zhai et al., 2013; Tu et al., 2015; Wang et al., 2015), even if degradation of passenger strands is postulated to explain their poor stability compared with guide strands. Supporting the need for rapid passenger strand clearing is the example of the fly C3PO endoribonuclease that facilitates RNAi by degrading passenger strand cleavage products (Liu et al., 2009). Since these products are observed only in the frame of the *ago1-57* mutated AGO1, this implies a rapid turnover by exoribonuclease activity in the wild type, while a slowed down process of unwinding protects the extremities from this unknown nuclease in *ago1-57*. Further genetic studies combining, perhaps, the *ago1-57* mutant and candidate exoribonucleases will be needed to validate this idea.

The Degron Mediating AGO Degradation by the SCF^{P0} Provides a Tool for Functional Studies of Plant AGOs

Finally, our findings may also provide a tool to study the functions of AGO proteins in plants. Hence, ectopic or tissue-specific expression of P0 in plants is expected to deplete most, if not all, AGO proteins, while the *ago1-57* equivalent mutation is expected to confer resistance to P0-mediated degradation to most of them. If this holds true, it may allow dissecting the function of individual AGO members in a plant or in specific tissues or even developmental contexts. However, the main limit of this approach is that the *ago1-57* mutation partially impairs AGO protein activity. Searching for additional mutations in the identified AGO1 degron that may still impair the binding of SCF^{P0} but without affecting AGO activities would represent an achievable alternative.

METHODS

Plant Lines

Arabidopsis thaliana XVE:P0 (L21), *XVE:P0-myc*, and L1 (*35S:GUS*) stable lines have been described previously (Morel et al., 2002; Bortolamiol et al., 2007; Derrien et al., 2012). The missense mutants *ago1-38* (Gregory et al., 2008), *ago1-42* (Poulsen et al., 2013), *ago1-18* (Sorin et al., 2005), *ago1-49* (Poulsen et al., 2013), and *ago1-27* (Morel et al., 2002) have been described previously. Except for Supplemental Figures 1A and 1B, *sup149.1* was backcrossed thrice to the parental line *XVE:P0*. For introgression of the backcrossed *sup149.1* mutation into the L1 and *XVE:P0-myc* lines, doubly homozygous plants for the mutations of interest lacking the *XVE:P0* transgene were obtained and used for further experiments. Both the *XVE:P0* and the *XVE:P0-myc* T-DNA insertions have been localized by a TAIL-PCR-based strategy (Singer and Burke, 2003) and genotyping primers were designed accordingly (Supplemental Table 1).

Plant Growth Conditions and Chemical Treatments

For standard plant growth, seeds were directly sown on soil (Hawita Fruhstorfer) in trays and kept under a 12-h-light/12-h-dark regime for 14 d, then transferred in 16-h-light/8-h-dark growth chambers, under fluorescent light (Osram Biolux 49W/965). Pictures were taken at the indicated time. For in vitro culture, seeds were surface sterilized using ethanol, plated on growth medium (MS salts [Duchefa], 1% sucrose, and 0.8% agar, pH 5.7), stored 2 d at 4°C in the dark, and then transferred to a plant growth chamber under a 16-h-light/8-h-dark photoperiod (22°C/20°C).

For P0-myc induction during plant growth, MS-agar plates were supplemented with 10 μM β-estradiol, while for mock treatment, an equal amount of DMSO was used. Plates were then handled as indicated above, and seedlings were harvested 7 to 8 d after sowing for protein content analysis or 9 to 10 d after sowing for aerial and root growth measurements.

For kinetic induction of P0-myc, seedlings were grown as indicated above for 8 to 12 d, then transferred into liquid MS medium (Duchefa) +1% sucrose in sterile conditions and left on a rotator for 15 min (65 rpm). This step was repeated once and MS medium was then replaced with either MS + DMSO (mock), MS + 10 μM β-estradiol, or MS + 10 μM β-estradiol + 20 μM MLN4924. Immerged seedlings were then left in the growth chamber for the indicated period of time before harvest.

Arabidopsis Seed Mutagenesis and Scoring

A total of 15,000 seeds homozygous for the *XVE:P0* transgene (Bortolamiol et al., 2007) were incubated for 15 h at room temperature in 40 mL of 100 mM Na-phosphate pH 5, 5% DMSO, and 0.25% EMS (Sigma-Aldrich) and washed several times, first with 100 mM Na-thiosulfate, and then with water. M1 seeds were sown in soil and rendered plants that were allowed to self-fertilize, and M2 seeds were harvested and bulked from of 50 to 75 M1 plants. M2 seeds from 8000 to 10,000 M1 plants were collected. Next, 150,000 of the M2 seeds obtained were surface-sterilized, sown on vertical MS 1% agar plates with 2% sucrose and 5 μM β-estradiol and incubated for 10 d in growth chambers with a constant temperature of 22°C and 12-h-light photoperiod. M2 seedlings whose root length exceeded 2-fold the average size of their siblings on the same plate were considered as putative mutants and transferred into soil for propagation and backcrossing.

Mapping of the *sup149.1* Mutation

To map the mutation, 27 F2 plants derived from a *sup149.1* × L*er* outcross were subjected to linkage analysis with 26 SSLP and in/del markers polymorphic between Col-0 and L*er*. This low-resolution analysis was performed as previously described (Ponce et al., 1999, 2006) and allowed us to map the *sup149.1* mutation to a candidate interval flanked by the At1g32140 and At1g55300 genes. In addition, we selected 28 plants from the F2 of the *sup149.1* × L*er* cross that had long root on β-estradiol. In their F3 progeny, we confirmed the presence of the L21 transgene by PCR and that of the AGO1 protein by immunoblotting. Two F3 seeds from each selfed F2 plant was used to obtain a mapping population of 56 F3 plants, whose DNA was extracted, pooled, and massively sequenced. The whole genomes of Col-0 L21 and L*er* were also sequenced. Six G→A and C→T transitions were present in the candidate interval of the F3 plants derived from the *sup149.1* × L*er* cross but absent from the Col-0 reference genome sequence and those of Col-0 L21b and L*er*. Three of these mutations affected coding sequences, one of which within *AGO1*.

For next-generation sequencing, 18-d-old rosettes were collected (1 g) and ground in liquid nitrogen, and their DNA was purified using the DNeasy Plant Midi Kit (Qiagen), according to the manufacturer's instructions. For library preparation, 1.2 μg of DNA was used. Whole-genome sequencing was performed in an Ion Proton platform (Thermo Fisher Scientific) and returned single reads with an average length of 156 nucleotides. The single-end reads obtained were aligned to the TAIR10 Col-0 reference genome using the Torrent Suite Software (version 5.2.1; Thermo Fisher Scientific). The resulting alignment was visualized using Tablet (version 1.15.09.01; Milne et al., 2010).

Constructs

The AGO1 deletion constructs were generated by PCR amplification from the *AtAGO1* cDNA with the oligonucleotide primers listed in Supplemental Table 1. Amplicons were reamplified with oligos primers MD30 and MD31 (Supplemental Table 1) containing the attB sites and recombined into pDONR Zeo plasmids (Invitrogen). They were then transferred into the binary vector pK7FWG2 (Karimi et al., 2005) by Gateway LR reaction to create the final C-terminal GFP fusion placed under the regulation of the 35S promoter. The *35S:P19*, *35S:GUS*, and *35S:P0-myc* constructs have been described elsewhere (Baumberger et al., 2007).

The alanine *ΔNΔC-GFP* scanning constructs have been generated by a two-step megaprime PCR procedure performed on the ΔNΔC sequence. In a first step, primers containing the respective mutations (Supplemental Table 1) were used in combination with the Gateway primers MD30 or MD31, using the pK7FWG2-ΔNΔC vector as a DNA matrix to generate megaprimers containing the desired mutations. Megaprimers were then gel purified using NucleoSpin Gel and PCR clean-up kit (Macherey-Nagel) and resuspended in water. In a second step, the full-length sequence of mutagenized ΔNΔC fragments were generated by PCR using the respective megaprimers in combination with either the MD30 or MD31 primers and pK7FWG2-ΔNΔC as a DNA matrix. The mutagenized ΔNΔC fragments were then cloned in the Gateway vector pDONR ZEO (Invitrogen) by Gateway BP reaction and finally mobilized into the destination vector pK7FWG2 by Gateway LR reaction to create the C-terminal GFP fusion placed under the regulation of the 35S promoter.

For the *XVE:P0-LP1-myc* construct, the P0-LP1 (Pazhouhandeh et al., 2006) sequence was amplified with the P0dir and P0rev primers (Supplemental Table 1), digested with *Xba*I-*Pst*I, and cloned into a pKS vector. The resulting vector was *Xba*I-*Mfe*I digested and ligated with a *Eco*RI-*Bam*HI digested 3xMyc, to insert a Myc-tag in frame with the C terminus of the TuYV *P0-LP1* gene, and the construct was further introduced into the *Xho*I-*Spe*I sites of pER8 (Zuo et al., 2000) to produce *XVE:P0-myc-LP1*. The clone was then mobilized into *Agrobacterium tumefaciens* strain and used to transform Col-0 plants (Clough and Bent, 1998).

For the *pAGO2:Venus-AGO2g* construct, the *AGO2* promoter sequence and 5′ untranslated region (UTR; 1.3 kb) were first amplified from genomic DNA and seamlessly fused upstream of the coding sequence of the *Venus* gene (no stop) by three-way Gibson assembly reaction (NEB), into the pFK202 plasmid. The resulting construct was then seamlessly fused by a three-way Gibson assembly reaction to generate a construct in the following order: promoter–*Venus*–*AGO2* genomic part I–*AGO2* genomic part II, allowing for mutagenesis of G1261 to an A at the junction of the two parts. The wild-type counterpart was generated by inserting the whole ATG-AGO2 genomic-3′UTR in the *Spe*I-*Sac*I sites of the modified pFK202. Finally, *AGO2* promoter sequence and 5′UTR were introduced into the pDONR P4P1r vector by BP Gateway recombination (Invitrogen), while the *ATG-Venus-AGO2g* constructs were introduced into the pDONR221 by the same method. Pieces were assembled into the pK-7m24GW3 plasmid (http://www.psb.ugent.be/gateway/) by double recombination LR reaction (Invitrogen) to obtain the final binary plasmid. The plasmid was then mobilized into Agrobacterium strain GV3101 and used for transient expression assays in *Nicotiana benthamiana*. Primers are listed in Supplemental Table 1.

For cloning of the *sup149.1* mutation in NtAGO1, the *sup149.1* mutation was introduced in the pSP-Flag-NtAGO1 (pSP-ntFlAGO1) vector (Iki et al., 2010) using the overlap PCR method with the mutagenic primers ntago1sup149.1-fwd_2 and ntago1sup149.1-rev_2. After PCR amplification, the original vector was removed from the PCR mix by *Dpn*I restriction digestion. The mutated vector pSP-Flag-NtAGO1-sup149 was then transformed in *Escherichia coli* TOP10 cells.

For *35S:CFP-AGO1* constructs, the *AGO1* coding sequence was amplified with oligo primers containing the attB sites and the PCR product was subsequently cloned in a pDONR Zeo by BP recombination (Invitrogen). The resulting entry clone was mutagenized (Edelheit et al., 2009) with the primers listed in Supplemental Table 1, producing the G371→D and G186→R mutations. The entry clones were then recombined with the pB7WGC2 vector (Karimi et al., 2005) by LR gateway reaction (Invitrogen) producing 35S promoter driven *AGO1* constructs fused to CFP at their N termini.

Transient Expression Assays in *N. benthamiana*

Binary constructs were transformed in Agrobacterium GV3101 or C58C1 (*35S:P19*, *35S:GUS* and *35S:P0-myc*) and then transformed in *N. benthamiana* for transient expression assays. Agrobacterium cells were grown overnight at 28°C in 5 to 10 mL LB medium supplemented with antibiotics, resuspended in 10 mM $MgCl_2$ + 10 mM MES + 200 mM acetosyringone at an OD of 0.3 per construct, and incubated for 2 to 4 h at room temperature before being pressure-infiltrated into leaves of 4-week-old plants. Plants were maintained in growth chambers under a 16-h-light/8-h-dark photoperiod with a constant temperature of 22°C.

Protein Analysis and Immunoblotting

Total proteins were extracted from seedlings or from plant leaves using 2× Laemmli buffer. Ten to fifteen micrograms of total protein extracts were separated on SDS-PAGE gels and blotted onto Immobilon-P membrane (Millipore). AGO1 protein was detected using the anti-AGO1 antibody (rabbit polyclonal, AS09 527; Agrisera) diluted 1:10,000 (v/v). AGO2 protein was detected using the anti-AGO2 antibody (rabbit polyclonal, AS13 2682; Agrisera) diluted 1:5000 (v/v). AGO4 protein was detected using the anti-AGO4 antibody (rabbit polyclonal, AS09 617; Agrisera) diluted 1:5000 (v/v). SDE3 protein was detected using an anti-SDE3 antibody (rabbit polyclonal; Eurogentec) diluted 1:4000 (v/v) and gels were loaded with 35 μg of total protein extract per lane. Myc-tagged proteins were detected using anti-myc antibody (mouse monoclonal; Roche) diluted 1:5000 (v/v). Actin protein was detected using antiactin antibody (Agrisera; AS13 2640) diluted 1:15,000 (v/v). Cullin 1 protein was detected using anti-CUL1 antibody (Shen et al., 2002) diluted 1:5000. GFP-tagged proteins were detected using the anti-GFP antibody (rat monoclonal [3H9]; Chromotek) diluted 1:5000 (v/v). ASK1 protein was detected using the anti-ASK1 serum (Xu et al., 2002) diluted 1:2000 (v/v). RBX1 protein was detected using the anti-RBX1 antibody (Lechner et al., 2002) diluted 1:2000 (v/v). Flag-tagged proteins were detected using the anti-Flag HRP-linked antibody (mouse monoclonal, A8592; Sigma-Aldrich) diluted 1:5000 (v/v). Mouse monoclonal antibodies were detected with a goat anti-mouse IgG HRP-linked antibody (62-6520; Invitrogen) diluted 1/10,000 (v/v). Rat monoclonal antibody were detected with a goat anti-rat IgG HRP-linked Antibody (7077; Cell Signaling) diluted 1/5000 (v/v). Rabbit polyclonal antibody were detected with a goat anti-rabbit IgG HRP-linked antibody (65-6120; Invitrogen) diluted 1/10,000 (v/v). Hybridized membranes were reacted with ECL+ (Lumi-Light^{PLUS} Western Blotting; Roche) and imaged using ECL films, chemidoc touch (Bio-Rad), or Fusion FX (Vilbert).

RNA Analyses by RNA Gel Blotting, Native Gel, and RT-qPCR

RNA extraction was performed on 2-week-old Arabidopsis seedlings grown on MS agar plates, on leaves from 5-week-old Arabidopsis plants, or on Arabidopsis inflorescence using Tri-Reagent (Sigma-Aldrich) according to the manufacturer's instructions. RNA gel blot analyses of low molecular weight RNA were performed with 10 μg (seedlings), 40 μg (leaves), or 20 μg (flowers) of total RNA. Low molecular weight RNAs were resuspended in a final concentration of 60% formamide-5 mM EDTA-0.05% bromophenol blue-0.05% xylene cyanol, heated a 95°C for 5 min, and separated by electrophoresis on 15% polyacrylamide gels

(19:1 acrylamide:bisacrylamide)-8 M Urea-0.5× TBE gel. Separated RNA species were electroblotted on Hybond-NX (Amersham) membrane and fixed by a carbodiimide-mediated cross-linking procedure (Pall et al., 2007). DNA oligonucleotides complementary to small RNA and U6 (Supplemental Table 1) were end-labeled with [γ-^{32}P]ATP using T4 PNK (New England Biolabs). Hybridization was performed overnight in PerfectHyb Plus (Sigma-Aldrich) at 42°C and membranes were washed once in 2× SSC-2% SDS and twice in 1× SSC-1% SDS before exposure. For separation of high molecular weight RNA, total RNA was resuspended in 25% formamide-6% formaldehyde-0.5X MOPS-5% glycerol-0.025% bromophenol blue and xylene cyanol, heated at 95°C for 5 min, and separated by electrophoresis in 1.2% agarose gel with 20 mM MOPS, 8 mM sodium acetate, 1 mM EDTA, and 6% formaldehyde, pH 7. Separated RNA species were transferred onto Hybond-N$^+$ (Amersham) membrane overnight by capillarity and UV cross-linked. A PCR product (Supplemental Table 1) corresponding to the P0^{TuYV} sequence was used as a probe and 100 ng was used to obtain a [α-^{32}P]CTP-labeled Klenow product (prime-a-gene; Promega). Hybridization was performed overnight in PerfectHyb Plus (Sigma-Aldrich) at 50°C, and membranes were washed once in 2× SSC 2% SDS and twice in 0.5× SSC 0.5% SDS before exposure. For separation of in vivo double-stranded from single-stranded small RNA species, Immunoprecipitated RNA were [γ-^{32}P]ATP labeled by T4 polynucleotide kinase (Thermo Fisher Scientific) for 35 min at 37°C, Tri-Reagent extracted, and precipitated overnight at −20°C. The pellet was resuspended in 4:1 ultrapure water:loading buffer (50% glycerol, 50 mM Tris-HCl, pH 7.7, 5mM EDTA, and bromophenol blue) and directly loaded into a 17.5% native polyacrylamide-1× TBE gel, using 1× TBE as running buffer. Synthetic siR255/siR255* RNA oligos were used as a size control, either for double-stranded species (annealed and nondenatured) or single-stranded species (heat-treated before loading). The signals were detected using super RX-N (Fujifilm) x-ray films.

For quantitative RT-PCR, total RNA was extracted from 2-week-old seedlings grown on MS agar plates or from 5-week-old Arabidopsis plants using Tri-Reagent (see above). In all assays, 2 μg of total RNA treated with DNase I (Thermo Fisher Scientific) was reverse transcribed using Maxima First Strand cDNA Synthesis Kit (Thermo Fisher Scientific). Quantitative PCR reactions were performed in a total volume of 10 μL of KAPA SYBR FAST qPCR Master Mix LightCycler480 SDS (KAPABiosystem) on a Lightcycler LC480 apparatus (Roche) according to the manufacturer's instructions. The mean values of at least three biological replicates were normalized using the *ACTIN2* (AT3G18780), *TIP4* (AT4G34270), and AT4G26410 genes as internal controls.

Protein Immunoprecipitation

For immunoprecipitation of endogenous AGO1, frozen tissues were ground to a fine powder with a mortar and pestle, resuspended in 3 volumes of crude extract buffer (50 mM Tris, pH 7.5, 150 mM NaCl, 10% glycerol, 5 mM $MgCl_2$, 0.1% Igepal, 5 mM DTT, 10 μM MG132, and 1× Complete protease inhibitors cocktail [Roche]), and incubated for 20 min at 8 rpm in the cold room. Insoluble material was removed by centrifugation (twice 15 min, 16,000*g*, 4°C). Identical amounts of crude extracts were incubated with prebound @AGO1 (5 μg) PureProteome Protein A magnetic beads (30 μL; Millipore) for 1 h at 7 rpm in the cold room. Immune complexes were washed three times in the crude extract buffer, and purified small RNA was eluted from the beads in Tri-Reagent (Sigma-Aldrich). Extracted RNA was precipitated in 2 volumes of isopropanol + 40 μg glycogen overnight at −20°C. Pellets were resuspended in 60% formamide and analyzed by RNA gel blot as described above.

For immunoprecipitation of induced P0-myc protein, 400 mg of treated seedlings (as indicated above) was ground to a fine powder with a mortar and pestle, resuspended in 3 volumes of crude extract buffer (50 mM Tris, pH 7.5, 150 mM NaCl, 10% glycerol, 5 mM $MgCl_2$, 0.1% Igepal, 10 μM MG132, and 1× Complete protease inhibitors cocktail [Roche]), and incubated for 40 min at 8 rpm in the cold room. Insoluble material was removed by centrifugation (twice for 15 min, 16,000*g*, 4°C). Identical amounts of crude extracts were incubated with 50 μL μMACS anti cMyc magnetic beads (Miltenyi) for 1 h at 7 rpm in the cold room. Immune complexes were retained on μ Columns (Miltenyi) and washed four times in 550 μL crude extract buffer, and elution was performed by addition of 20 + 50 μL hot 1× Laemmli buffer on the column.

In Vitro RISC Loading Reaction

Small RNAs

The sequence information for 21- and 22-nucleotide miRNA and gf698 siRNAs is provided in Supplemental Table 1. All small RNAs had 2-hydroxymethyl groups on the 3-OH terminal nucleotides. The guide strands were phosphorylated in the presence of [γ-^{32}P]ATP by T4 polynucleotide kinase (Thermo Fisher Scientific), while the passenger strands were also phosphorylated but without radiolabeling. The annealing was performed during the incubation at 96°C for 2 min followed by a gradual temperature decrease in the annealing buffer composed of 10 mM Tris-HCl (pH 7.6), 20 mM KCl, and 1 mM $MgCl_2$.

In Vitro Translation

The preparation of BYL and in vitro translation reaction were done as described previously (Komoda et al., 2004). Membranous fraction of BYL was pelleted by centrifugation (15,000*g*, 15 min), and the cytosolic fraction (S15) was then passed through a G25 column (GE Healthcare). Eluate of the S15 through the G25 column was then used for preparation of the in vitro translation mixture. All mRNAs were translated at a final concentration of 0.05 μg/μL in the reaction mixtures. mRNAs were prepared using linearized pSP-Flag-NtAGO1 and pSP-Flag-NtAGO1-ago1-57 vector as DNA matrix for in vitro transcription reactions, which were performed with the Amplicap SP6 kit (Cambio) according to the manufacturer's instructions.

RISC Loading Reaction

After in vitro translation of *NtAGO1*, and *NtAGO1$^{ago1\text{-}57}$* mRNAs in BYL, reaction mixtures were incubated at 25°C for 60 min with 10 nM miRNA or gf698 siRNA duplexes containing 5′ ^{32}P-labeled guide strand in the additional presence of ATP-regenerating system composed of 0.75 mM ATP, 1 mM $MgCl_2$, 20 mg/mL creatine phosphate, and 0.4 mg/mL creatine kinase. To analyze RNA, the reaction mixtures were then diluted 10-fold with 10 mM Tris and 1 mM EDTA (TE, pH 8.0) and extracted with equal volumes of phenol chloroform isoamyl alcohol (PCI; 25:24:1, v/v). The resulting aqueous phase was recovered and mixed with an equal volume of the native loading dye solution (1× TBE, 10% [v/v] glycerol, bromophenol blue, and xylene cyanol). To analyze NtAGO1 and NtAGO1$^{ago1\text{-}57}$ loaded sRNA, samples were mixed with 10 μL (packed volume) of ANTI-FLAG M2 magnetic beads (Sigma-Aldrich) equilibrated in 100 μL of TR buffer [30 mM HEPES, pH 7.4, 80 mM KOAc, 1.8 mM $Mg(Oac)_2$, 2 mM DTT, and 1× Complete protease inhibitors cocktail (Roche)] and incubated on ice for 60 min with occasional swirling. Then, the beads were washed three times with TR buffer and bead-associated RNAs were extracted by adding TE and PCI (1:1 v/v). Immunoprecipitated RNA was then run on a 15% native PAGE using 0.5× TBE as running buffer (150 V, 40 min). The signals were detected using BAS-MS imaging plate (FUJIFILM) and a Typhoon FLA 9000 image analyzer (GE Healthcare).

GUS Activity Measurements

GUS quantification was done as previously described (Martínez de Alba et al., 2011). Activity is expressed as fluorescence units per minute per

microgram of total protein in the extract, as quantified by Bradford assay. Both L1 mother line and L1 siblings obtained from the segregating population are shown as control. Six individual plants grown in soil for 45 d from each genotype were analyzed.

sRNA Library Preparation

Total-RNA samples were extracted from 2-week-old seedlings grown on MS-agar plates using Tri-Reagent according to the manufacturer's instruction. For AGO1-loaded sRNA samples, IPs were performed as described in the supplemental files from 300 mg of 2-week-old seedlings grown on MS-agar plates. AGO1-loaded sRNAs were then extracted by adding Tri-Reagent directly on the magnetic beads and extraction of RNA was then performed according to the manufacturer's instructions. RNA samples were sent to Fasteris (http://www.fasteris.com) for library preparation and sRNA sequencing on an Illumina HiSeq sequencer. For total-RNA library preparation, 3 μg of total RNA from each sample was sent to Fasteris and for AGO1 loaded sRNA the total amount of RNA recovered from each IP were used. For each condition, two biological replicates were processed and to reduce technical variability, each sample was split and sequenced in two independent lanes. FASTQ file generation, demultiplexing, and adapter removal were done by Fasteris. These deep sequencing files have been deposited to the NCBI Gene Expression Omnibus (GSE104015).

sRNA Sequencing Data Processing

sRNA Mapping

Reads (18 to 35 nucleotides long) with identical sequences were grouped using the processReads function from the ncPRO-seq pipeline (Chen et al., 2012) and aligned against the Arabidopsis genome (TAIR10) using bowtie2 (Langmead and Salzberg, 2012). Mapping statistics are provided in Supplemental Figure 4A.

Differential Analysis

Reads (20 to 24 nucleotides long) whose genomic position were nested TAIR10 and miRBaseV21 mature miRNA annotations were counted for each sRNA-seq libraries using in house python script (mature miRNA annotations were enlarged by 2 nucleotides up- and downstream). Raw count corresponding to loci annotated as genes, pseudogenes, tasiRNA, other RNA, and mature miRNA were used for differential analysis between Col-0 wild-type and *ago1-57* mutant libraries using DEseq2 v1.12.4 (Love et al., 2014). Loci with an adjusted P value lower than 0.05 were considered as having differential sRNA accumulation as represented in the MAplot in Figures 6A and 6B (Supplemental Data Set 1) and were used for further analysis (Figure 7B; Supplemental Figures 4B to 4D).

sRNA Profile and Phasing along Loci

Simple genomic position comparison was applied to retrieve 18- to 35-nucleotide-long sRNA read counts and positions corresponding to the selected loci. Those were then used to calculate the normalized read counts (reads per 10 million reads) for each nucleotide and to produce a graphical representation using R (packages Cairo and ggplot2) based on the mean of the two replicates. Positions of miRNA target sites were retrieved from the *Arabidopsis thaliana* Small RNA project (ASRP) genome browser (http://asrp.danforthcenter.org/athaliana). Position of siRNA target sites for ath-siR2140/TAS2-3′D6- were retrieved from the tasiRNAdb of the Bioinformatics Center in Jinling Institut of Technology (http://bioinfo.jit.edu.cn). Position of siRNA target for atTAS8-siR9as was retrieved manually using the GBrowser from TAIR (https://gbrowse.arabidopsis.org).

Phasing analysis was done retrieving 21-nucleotide-long reads corresponding to the selected locus and calculating the proportion of reads in each of the 21-phase register for the plus and minus strands. Graphical representations presented in Figure 7B and Supplemental Figure 5 have been done by applying the radial.plot function from R plotrix package.

Hierarchical Clustering of Mature miRNA between Col-0 Wild Type and ago1-57 Libraries

sRNA reads (20 to 24 nucleotides) corresponding to mature miRNA annotations (miRBase V21) enlarged by two nucleotides up- and downstream were counted and normalized by library size as well as by the number of genomic position of each sRNA sequence. Average normalized reads count and log fold change between Col-0 and *ago1-57* were calculated after transformation into pseudocount (adding +1 to each loci). Only miRNA with an average value of at least 10 and log fold change higher or lower than 1 are represented. Hierarchical clustering (Ward.D) is based on the Manhattan distance of the log fold change, and the color scale is normalized by row in order to allow libraries comparison and avoid miRNA to miRNA comparison. Graphical representations provided in Supplemental Figure 4E have been generated using R (package heatmap2).

Comparative Modeling

Arabidopsis AGO1 structural models have been generated using the PHYRE2 server (Kelley et al., 2015). The AtAGO1 peptide sequence (UniProtKB/Swiss-Prot: O04379.1) has been submitted to PHYRE2 server for 3D protein structure modeling. Molecular graphics and analyses were performed with the UCSF Chimera package. Chimera is developed by the Resource for Biocomputing, Visualization, and Informatics at the University of California, San Francisco (supported by NIGMS P41-GM103311) (Pettersen et al., 2004). The PyMOL Molecular Graphics System, version 1.7.4.5 (Schrödinger), was used to generate Supplemental Movie 1. Domains were color-coded as indicated in the legend.

Protein Sequence Alignments

AGO sequences were retrieved from GenBank by BLASTp, using the full AGO1 protein sequence as query. Retrieved sequences were aligned using the multiple sequence comparison by log expectation (MUSCLE) packaged in Unipro UGENE v1.26.2. The resulting alignment was exported as an image file. Species used for the alignments are indicated in Supplemental Figure 2A: *At*, *Arabidopsis thaliana*; *Pt*, *Populus trichocarpa*; *Sl*, *Solanum lycopersicum*; *Nt*, *Nicotiana tabacum*; *Os*, *Oryza sativa*; *Bd*, *Brachypodium distachyon*; *Cr*, *Chlamydomonas reinhardtii*; *Hs*, *Homo sapiens*; *Mm*, *Mus musculus*; *Rn*, *Rattus norvegicus*; *Dm*, *Drosophila melanogaster*; *Am*, *Apis mellifera*; *Ce, Caenorhabditis elegans*; *Sp*, *Schizosaccharomyces pombe*

Accession Numbers

Sequence data from this article can be found in the Arabidopsis Genome Initiative or GenBank/EMBL databases under the following accession numbers: *AGO1*, At1g48410; *AGO2*, At1g31280; *AGO4*, At2g27040; *CUL1*, At4g02570; *ASK1*, At1G75950; and *RBX1*, At5g20570. P0 sequence used in this study is from the *Turnip yellow virus* (BWYV-FL1) genomic RNA (GenBank ID X13063.1).

Supplemental Data

Supplemental Figure 1. Molecular analysis of selected P0 suppressor lines.

Supplemental Figure 2. Alignment of amino acid sequences DUF1785 region of eukaryotic AGOs and the ability of SCF^{P0} to associate with an AGO1 point mutant.

Supplemental Figure 3. Phenotypic defects observed in *ago1* point mutants.

Supplemental Figure 4. miRNA abundance in wild type versus *ago1-57* mutant from RNA-seq libraries.

Supplemental Figure 5. Phasing of the TAS loci is conserved in the *ago1-57* mutant.

Supplemental Table 1. List of the oligos primers and probes used in this study.

Supplemental File 1. Source images for blots in Figures 1, 2, 3, and 6.

Supplemental Movie 1. Predictive structural model of Arabidopsis AGO1 and the P0 degron.

Supplemental Data Set 1A. Loci underaccumulating 20- to 24-nucleotide-long sRNA reads in the *ago1-57* mutant compared with Col-0, according to small RNA sequencing performed on total RNA samples.

Supplemental Data Set 1B. Loci underaccumulating 20- to 24-nucleotide-long sRNA reads in the *ago1-57* mutant compared with Col-0, according to small RNA sequencing performed on AGO1-immunoprecipitated RNA samples.

Supplemental Data Set 1C. Loci overaccumulating 20- to 24-nucleotide-long sRNA reads in the *ago1-57* mutant compared with Col-0, according to small RNA sequencing performed on total RNA samples.

Supplemental Data Set 1D. Loci overaccumulating 20- to 24-nucleotide-long sRNA reads in the *ago1-57* mutant compared with Col-0, according to small RNA sequencing performed on AGO1-immunoprecipitated RNA samples.

ACKNOWLEDGMENTS

We thank K. Hleibieh for technical support for the P0 suppressor screen, Nathalie Bouteiller for GUS measurements, Julia De Cillia for gift of the XVE:P0-myc LP1 line, Diana Navarro-Martínez, and Raquel Sarmiento-Mañús for expert technical help with the mapping-by-sequencing of the *sup149.1* mutation. P.G. acknowledges support from the European Research Council under the European Union's Seventh Framework Programme (FP7/2007-2013)/European Research Council advanced Grant 338904, and from the Agence Nationale de la Recherche LABEX, ANR-10-LABX-0036_NETRNA. J.L.M. and M.R.P. were supported by grants from the Ministerio de Economía y Competitividad of Spain (BIO2014-53063-P to J.L.M. and BIO2104-56889-R to M.R.P.) and the Generalitat Valenciana (PROMETEOII/2014/006 to J.L.M.). O.V., T.I., and A.S. were supported by a core grant from the ETH-Zürich, an IIF Marie Curie fellowship from the European Commission to T.I. (329029), and European Research Council advanced grant to O.V. ("Frontiers of RNAi-II" number 323071).

AUTHOR CONTRIBUTIONS

B.D., M.C., T.I., and P.G. designed research. B.D., M.C., N.B., T.I., T.H., M.R.P., V.Z.G., H.V., and J.L.M. performed research. B.D., M.C., T.I., A.S., H.V., O.V., and J.L.M. analyzed the data. B.D., M.C., and P.G. wrote the article, with help from T.I., A.S., H.V., O.V., and J.L.M.

Received February 7, 2018; revised April 19, 2018; accepted May 18, 2018; published May 30, 2018.

REFERENCES

Almasi, R., Miller, W.A., and Ziegler-Graff, V. (2015). Mild and severe cereal yellow dwarf viruses differ in silencing suppressor efficiency of the P0 protein. Virus Res. **208:** 199–206.

Arribas-Hernández, L., Kielpinski, L.J., and Brodersen, P. (2016a). mRNA decay of most Arabidopsis miRNA targets requires slicer activity of AGO1. Plant Physiol. **171:** 2620–2632.

Arribas-Hernández, L., Marchais, A., Poulsen, C., Haase, B., Hauptmann, J., Benes, V., Meister, G., and Brodersen, P. (2016b). The slicer activity of ARGONAUTE1 is required specifically for the phasing, not production, of trans-acting short interfering RNAs in Arabidopsis. Plant Cell **28:** 1563–1580.

Baumberger, N., and Baulcombe, D.C. (2005). Arabidopsis ARGONAUTE1 is an RNA Slicer that selectively recruits microRNAs and short interfering RNAs. Proc. Natl. Acad. Sci. USA **102:** 11928–11933.

Baumberger, N., Tsai, C.H., Lie, M., Havecker, E., and Baulcombe, D.C. (2007). The Polerovirus silencing suppressor P0 targets ARGONAUTE proteins for degradation. Curr. Biol. **17:** 1609–1614.

Bologna, N.G., and Voinnet, O. (2014). The diversity, biogenesis, and activities of endogenous silencing small RNAs in Arabidopsis. Annu. Rev. Plant Biol. **65:** 473–503.

Borges, F., and Martienssen, R.A. (2015). The expanding world of small RNAs in plants. Nat. Rev. Mol. Cell Biol. **16:** 727–741.

Bortolamiol, D., Pazhouhandeh, M., Marrocco, K., Genschik, P., and Ziegler-Graff, V. (2007). The Polerovirus F box protein P0 targets ARGONAUTE1 to suppress RNA silencing. Curr. Biol. **17:** 1615–1621.

Brodersen, P., Sakvarelidze-Achard, L., Bruun-Rasmussen, M., Dunoyer, P., Yamamoto, Y.Y., Sieburth, L., and Voinnet, O. (2008). Widespread translational inhibition by plant miRNAs and siRNAs. Science **320:** 1185–1190.

Brodersen, P., Sakvarelidze-Achard, L., Schaller, H., Khafif, M., Schott, G., Bendahmane, A., and Voinnet, O. (2012). Isoprenoid biosynthesis is required for miRNA function and affects membrane association of ARGONAUTE 1 in Arabidopsis. Proc. Natl. Acad. Sci. USA **109:** 1778–1783.

Candela, H., Casanova-Sáez, R., and Micol, J.L. (2015). Getting started in mapping-by-sequencing. J. Integr. Plant Biol. **57:** 606–612.

Cascardo, R.S., Arantes, I.L., Silva, T.F., Sachetto-Martins, G., Vaslin, M.F., and Corrêa, R.L. (2015). Function and diversity of P0 proteins among cotton leafroll dwarf virus isolates. Virol. J. **12:** 123.

Chapman, E.J., Prokhnevsky, A.I., Gopinath, K., Dolja, V.V., and Carrington, J.C. (2004). Viral RNA silencing suppressors inhibit the microRNA pathway at an intermediate step. Genes Dev. **18:** 1179–1186.

Chen, C.J., Servant, N., Toedling, J., Sarazin, A., Marchais, A., Duvernois-Berthet, E., Cognat, V., Colot, V., Voinnet, O., Heard, E., Ciaudo, C., and Barillot, E. (2012). ncPRO-seq: a tool for annotation and profiling of ncRNAs in sRNA-seq data. Bioinformatics **28:** 3147–3149.

Chen, H.M., Li, Y.H., and Wu, S.H. (2007). Bioinformatic prediction and experimental validation of a microRNA-directed tandem trans-acting siRNA cascade in Arabidopsis. Proc. Natl. Acad. Sci. USA **104:** 3318–3323.

Clough, S.J., and Bent, A.F. (1998). Floral dip: a simplified method for Agrobacterium-mediated transformation of Arabidopsis thaliana. Plant J. **16:** 735–743.

Csorba, T., Lózsa, R., Hutvágner, G., and Burgyán, J. (2010). Polerovirus protein P0 prevents the assembly of small RNA-containing RISC complexes and leads to degradation of ARGONAUTE1. Plant J. **62:** 463–472.

Csorba, T., Kontra, L., and Burgyán, J. (2015). viral silencing suppressors: Tools forged to fine-tune host-pathogen coexistence. Virology **479-480:** 85–103.

Cuperus, J.T., Carbonell, A., Fahlgren, N., Garcia-Ruiz, H., Burke, R.T., Takeda, A., Sullivan, C.M., Gilbert, S.D., Montgomery, T.A., and Carrington, J.C. (2010). Unique functionality of 22-nt miRNAs in triggering RDR6-dependent siRNA biogenesis from target transcripts in Arabidopsis. Nat. Struct. Mol. Biol. **17:** 997–1003.

Derrien, B., Baumberger, N., Schepetilnikov, M., Viotti, C., De Cillia, J., Ziegler-Graff, V., Isono, E., Schumacher, K., and Genschik, P.

(2012). Degradation of the antiviral component ARGONAUTE1 by the autophagy pathway. Proc. Natl. Acad. Sci. USA **109:** 15942–15946.

Ding, S.W. (2010). RNA-based antiviral immunity. Nat. Rev. Immunol. **10:** 632–644.

Eamens, A.L., Smith, N.A., Curtin, S.J., Wang, M.B., and Waterhouse, P.M. (2009). The Arabidopsis thaliana double-stranded RNA binding protein DRB1 directs guide strand selection from microRNA duplexes. RNA **15:** 2219–2235.

Edelheit, O., Hanukoglu, A., and Hanukoglu, I. (2009). Simple and efficient site-directed mutagenesis using two single-primer reactions in parallel to generate mutants for protein structure-function studies. BMC Biotechnol. **9:** 61.

Elkayam, E., Kuhn, C.D., Tocilj, A., Haase, A.D., Greene, E.M., Hannon, G.J., and Joshua-Tor, L. (2012). The structure of human argonaute-2 in complex with miR-20a. Cell **150:** 100–110.

Fei, Q., Xia, R., and Meyers, B.C. (2013). Phased, secondary, small interfering RNAs in posttranscriptional regulatory networks. Plant Cell **25:** 2400–2415.

Fusaro, A.F., Correa, R.L., Nakasugi, K., Jackson, C., Kawchuk, L., Vaslin, M.F., and Waterhouse, P.M. (2012). The Enamovirus P0 protein is a silencing suppressor which inhibits local and systemic RNA silencing through AGO1 degradation. Virology **426:** 178–187.

Garcia, D., Garcia, S., Pontier, D., Marchais, A., Renou, J.P., Lagrange, T., and Voinnet, O. (2012). Ago hook and RNA helicase motifs underpin dual roles for SDE3 in antiviral defense and silencing of nonconserved intergenic regions. Mol. Cell **48:** 109–120.

Ghildiyal, M., and Zamore, P.D. (2009). Small silencing RNAs: an expanding universe. Nat. Rev. Genet. **10:** 94–108.

Gibbings, D., Mostowy, S., Jay, F., Schwab, Y., Cossart, P., and Voinnet, O. (2012). Selective autophagy degrades DICER and AGO2 and regulates miRNA activity. Nat. Cell Biol. **14:** 1314–1321.

Gregory, B.D., O'Malley, R.C., Lister, R., Urich, M.A., Tonti-Filippini, J., Chen, H., Millar, A.H., and Ecker, J.R. (2008). A link between RNA metabolism and silencing affecting Arabidopsis development. Dev. Cell **14:** 854–866.

Gu, S., Jin, L., Huang, Y., Zhang, F., and Kay, M.A. (2012). Slicing-independent RISC activation requires the argonaute PAZ domain. Curr. Biol. **22:** 1536–1542.

Howell, M.D., Fahlgren, N., Chapman, E.J., Cumbie, J.S., Sullivan, C.M., Givan, S.A., Kasschau, K.D., and Carrington, J.C. (2007). Genome-wide analysis of the RNA-DEPENDENT RNA POLYMERASE6/DICER-LIKE4 pathway in Arabidopsis reveals dependency on miRNA- and tasiRNA-directed targeting. Plant Cell **19:** 926–942.

Iki, T., Yoshikawa, M., Nishikiori, M., Jaudal, M.C., Matsumoto-Yokoyama, E., Mitsuhara, I., Meshi, T., and Ishikawa, M. (2010). In vitro assembly of plant RNA-induced silencing complexes facilitated by molecular chaperone HSP90. Mol. Cell **39:** 282–291.

Iki, T., Ishikawa, M., and Yoshikawa, M. (2017). In vitro formation of plant RNA-induced silencing complexes using an extract of evacuolated tobacco protoplasts. Methods Mol. Biol. **1640:** 39–53.

Iwasaki, S., Kobayashi, M., Yoda, M., Sakaguchi, Y., Katsuma, S., Suzuki, T., and Tomari, Y. (2010). Hsc70/Hsp90 chaperone machinery mediates ATP-dependent RISC loading of small RNA duplexes. Mol. Cell **39:** 292–299.

Iwasaki, S., Sasaki, H.M., Sakaguchi, Y., Suzuki, T., Tadakuma, H., and Tomari, Y. (2015). Defining fundamental steps in the assembly of the Drosophila RNAi enzyme complex. Nature **521:** 533–536.

Karimi, M., De Meyer, B., and Hilson, P. (2005). Modular cloning in plant cells. Trends Plant Sci. **10:** 103–105.

Kawamata, T., Seitz, H., and Tomari, Y. (2009). Structural determinants of miRNAs for RISC loading and slicer-independent unwinding. Nat. Struct. Mol. Biol. **16:** 953–960.

Kelley, L.A., Mezulis, S., Yates, C.M., Wass, M.N., and Sternberg, M.J. (2015). The Phyre2 web portal for protein modeling, prediction and analysis. Nat. Protoc. **10:** 845–858.

Ketting, R.F., Fischer, S.E., Bernstein, E., Sijen, T., Hannon, G.J., and Plasterk, R.H. (2001). Dicer functions in RNA interference and in synthesis of small RNA involved in developmental timing in *C. elegans.* Genes Dev. **15:** 2654–2659.

Komoda, K., Naito, S., and Ishikawa, M. (2004). Replication of plant RNA virus genomes in a cell-free extract of evacuolated plant protoplasts. Proc. Natl. Acad. Sci. USA **101:** 1863–1867.

Krol, J., Loedige, I., and Filipowicz, W. (2010). The widespread regulation of microRNA biogenesis, function and decay. Nat. Rev. Genet. **11:** 597–610.

Kwak, P.B., and Tomari, Y. (2012). The N domain of Argonaute drives duplex unwinding during RISC assembly. Nat. Struct. Mol. Biol. **19:** 145–151.

Langmead, B., and Salzberg, S.L. (2012). Fast gapped-read alignment with Bowtie 2. Nat. Methods **9:** 357–359.

Lechner, E., Xie, D., Grava, S., Pigaglio, E., Planchais, S., Murray, J.A., Parmentier, Y., Mutterer, J., Dubreucq, B., Shen, W.H., and Genschik, P. (2002). The AtRbx1 protein is part of plant SCF complexes, and its down-regulation causes severe growth and developmental defects. J. Biol. Chem. **277:** 50069–50080.

Leung, A.K., and Sharp, P.A. (2010). MicroRNA functions in stress responses. Mol. Cell **40:** 205–215.

Leuschner, P.J., Ameres, S.L., Kueng, S., and Martinez, J. (2006). Cleavage of the siRNA passenger strand during RISC assembly in human cells. EMBO Rep. **7:** 314–320.

Li, S., et al. (2013). MicroRNAs inhibit the translation of target mRNAs on the endoplasmic reticulum in Arabidopsis. Cell **153:** 562–574.

Li, S., et al. (2016). Biogenesis of phased siRNAs on membrane-bound polysomes in Arabidopsis. eLife **5:** e22750.

Liu, Q., Rand, T.A., Kalidas, S., Du, F., Kim, H.E., Smith, D.P., and Wang, X. (2003). R2D2, a bridge between the initiation and effector steps of the Drosophila RNAi pathway. Science **301:** 1921–1925.

Liu, Y., Ye, X., Jiang, F., Liang, C., Chen, D., Peng, J., Kinch, L.N., Grishin, N.V., and Liu, Q. (2009). C3PO, an endoribonuclease that promotes RNAi by facilitating RISC activation. Science **325:** 750–753.

Love, M.I., Huber, W., and Anders, S. (2014). Moderated estimation of fold change and dispersion for RNA-seq data with DESeq2. Genome Biol. **15:** 550.

Maillard, P.V., Ciaudo, C., Marchais, A., Li, Y., Jay, F., Ding, S.W., and Voinnet, O. (2013). Antiviral RNA interference in mammalian cells. Science **342:** 235–238.

Martínez de Alba, A.E., Jauvion, V., Mallory, A.C., Bouteiller, N., and Vaucheret, H. (2011). The miRNA pathway limits AGO1 availability during siRNA-mediated PTGS defense against exogenous RNA. Nucleic Acids Res. **39:** 9339–9344.

Matranga, C., Tomari, Y., Shin, C., Bartel, D.P., and Zamore, P.D. (2005). Passenger-strand cleavage facilitates assembly of siRNA into Ago2-containing RNAi enzyme complexes. Cell **123:** 607–620.

Meister, G. (2013). Argonaute proteins: functional insights and emerging roles. Nat. Rev. Genet. **14:** 447–459.

Mi, S., et al. (2008). Sorting of small RNAs into Arabidopsis argonaute complexes is directed by the 5′ terminal nucleotide. Cell **133:** 116–127.

Milne, I., Bayer, M., Cardle, L., Shaw, P., Stephen, G., Wright, F., and Marshall, D. (2010). Tablet--next generation sequence assembly visualization. Bioinformatics **26:** 401–402.

Morel, J.B., Godon, C., Mourrain, P., Béclin, C., Boutet, S., Feuerbach, F., Proux, F., and Vaucheret, H. (2002). Fertile hypomorphic ARGONAUTE (ago1) mutants impaired in post-transcriptional gene silencing and virus resistance. Plant Cell **14:** 629–639.

Nodine, M.D., and Bartel, D.P. (2010). MicroRNAs prevent precocious gene expression and enable pattern formation during plant embryogenesis. Genes Dev. **24:** 2678–2692.

Okamura, K., Liu, N., and Lai, E.C. (2009). Distinct mechanisms for microRNA strand selection by Drosophila Argonautes. Mol. Cell **36:** 431–444.

Pall, G.S., Codony-Servat, C., Byrne, J., Ritchie, L., and Hamilton, A. (2007). Carbodiimide-mediated cross-linking of RNA to nylon membranes improves the detection of siRNA, miRNA and piRNA by northern blot. Nucleic Acids Res. **35:** e60.

Parent, J.S., Bouteiller, N., Elmayan, T., and Vaucheret, H. (2015). Respective contributions of Arabidopsis DCL2 and DCL4 to RNA silencing. Plant J. **81:** 223–232.

Park, J.H., and Shin, C. (2015). Slicer-independent mechanism drives small-RNA strand separation during human RISC assembly. Nucleic Acids Res. **43:** 9418–9433.

Pazhouhandeh, M., Dieterle, M., Marrocco, K., Lechner, E., Berry, B., Brault, V., Hemmer, O., Kretsch, T., Richards, K.E., Genschik, P., and Ziegler-Graff, V. (2006). F-box-like domain in the polerovirus protein P0 is required for silencing suppressor function. Proc. Natl. Acad. Sci. USA **103:** 1994–1999.

Peragine, A., Yoshikawa, M., Wu, G., Albrecht, H.L., and Poethig, R.S. (2004). SGS3 and SGS2/SDE1/RDR6 are required for juvenile development and the production of trans-acting siRNAs in Arabidopsis. Genes Dev. **18:** 2368–2379.

Pettersen, E.F., Goddard, T.D., Huang, C.C., Couch, G.S., Greenblatt, D.M., Meng, E.C., and Ferrin, T.E. (2004). UCSF Chimera--a visualization system for exploratory research and analysis. J. Comput. Chem. **25:** 1605–1612.

Ponce, M.R., Robles, P., and Micol, J.L. (1999). High-throughput genetic mapping in Arabidopsis thaliana. Mol. Gen. Genet. **261:** 408–415.

Ponce, M.R., Robles, P., Lozano, F.M., Brotóns, M.A., and Micol, J.L. (2006). Low resolution mapping of untagged mutations. In Arabidopsis protocols, 2nd ed: Methods in Molecular Biology, J. Salinas, and J.J. Sánchez-Serrano, eds (Totowa, NJ: Humana Press), pp. 105–113.

Poulsen, C., Vaucheret, H., and Brodersen, P. (2013). Lessons on RNA silencing mechanisms in plants from eukaryotic argonaute structures. Plant Cell **25:** 22–37.

Pumplin, N., and Voinnet, O. (2013). RNA silencing suppression by plant pathogens: defence, counter-defence and counter-counter-defence. Nat. Rev. Microbiol. **11:** 745–760.

Ramachandran, V., and Chen, X. (2008). Degradation of microRNAs by a family of exoribonucleases in Arabidopsis. Science **321:** 1490–1492.

Schirle, N.T., and MacRae, I.J. (2012). The crystal structure of human Argonaute2. Science **336:** 1037–1040.

Schneeberger, K., and Weigel, D. (2011). Fast-forward genetics enabled by new sequencing technologies. Trends Plant Sci. **16:** 282–288.

Shen, W.H., Parmentier, Y., Hellmann, H., Lechner, E., Dong, A., Masson, J., Granier, F., Lepiniec, L., Estelle, M., and Genschik, P. (2002). Null mutation of AtCUL1 causes arrest in early embryogenesis in Arabidopsis. Mol. Biol. Cell **13:** 1916–1928.

Singer, T., and Burke, E. (2003). High-throughput TAIL-PCR as a tool to identify DNA flanking insertions. Methods Mol. Biol. **236:** 241–272.

Sorin, C., Bussell, J.D., Camus, I., Ljung, K., Kowalczyk, M., Geiss, G., McKhann, H., Garcion, C., Vaucheret, H., Sandberg, G., and Bellini, C. (2005). Auxin and light control of adventitious rooting in Arabidopsis require ARGONAUTE1. Plant Cell **17:** 1343–1359.

Tomari, Y., Matranga, C., Haley, B., Martinez, N., and Zamore, P.D. (2004). A protein sensor for siRNA asymmetry. Science **306:** 1377–1380.

Tu, B., et al. (2015). Distinct and cooperative activities of HESO1 and URT1 nucleotidyl transferases in microRNA turnover in Arabidopsis. PLoS Genet. **11:** e1005119.

Varshavsky, A. (1991). Naming a targeting signal. Cell **64:** 13–15.

Vaucheret, H., Vazquez, F., Crété, P., and Bartel, D.P. (2004). The action of ARGONAUTE1 in the miRNA pathway and its regulation by the miRNA pathway are crucial for plant development. Genes Dev. **18:** 1187–1197.

Vazquez, F., Gasciolli, V., Crété, P., and Vaucheret, H. (2004). The nuclear dsRNA binding protein HYL1 is required for microRNA accumulation and plant development, but not posttranscriptional transgene silencing. Curr. Biol. **14:** 346–351.

Wang, X., Zhang, S., Dou, Y., Zhang, C., Chen, X., Yu, B., and Ren, G. (2015). Synergistic and independent actions of multiple terminal nucleotidyl transferases in the 3′ tailing of small RNAs in Arabidopsis. PLoS Genet. **11:** e1005091.

Wang, Y., Juranek, S., Li, H., Sheng, G., Tuschl, T., and Patel, D.J. (2008). Structure of an argonaute silencing complex with a seed-containing guide DNA and target RNA duplex. Nature **456:** 921–926.

Wang, Y., Juranek, S., Li, H., Sheng, G., Wardle, G.S., Tuschl, T., and Patel, D.J. (2009). Nucleation, propagation and cleavage of target RNAs in Ago silencing complexes. Nature **461:** 754–761.

Xu, L., Liu, F., Lechner, E., Genschik, P., Crosby, W.L., Ma, H., Peng, W., Huang, D., and Xie, D. (2002). The SCF(COI1) ubiquitin-ligase complexes are required for jasmonate response in Arabidopsis. Plant Cell **14:** 1919–1935.

Ye, R., Wang, W., Iki, T., Liu, C., Wu, Y., Ishikawa, M., Zhou, X., and Qi, Y. (2012). Cytoplasmic assembly and selective nuclear import of Arabidopsis Argonaute4/siRNA complexes. Mol. Cell **46:** 859–870.

Yoda, M., Kawamata, T., Paroo, Z., Ye, X., Iwasaki, S., Liu, Q., and Tomari, Y. (2010). ATP-dependent human RISC assembly pathways. Nat. Struct. Mol. Biol. **17:** 17–23.

Zhai, J., et al. (2013). Plant microRNAs display differential 3′ truncation and tailing modifications that are ARGONAUTE1 dependent and conserved across species. Plant Cell **25:** 2417–2428.

Zhang, X., Zhao, H., Gao, S., Wang, W.C., Katiyar-Agarwal, S., Huang, H.D., Raikhel, N., and Jin, H. (2011). Arabidopsis Argonaute 2 regulates innate immunity via miRNA393(*)-mediated silencing of a Golgi-localized SNARE gene, MEMB12. Mol. Cell **42:** 356–366.

Zuo, J., Niu, Q.-W., and Chua, N.-H. (2000). An estrogen-based transactivator XVE mediates highly inducible gene expression in transgenic plants. Plant J. **24:** 265–273.